

2D Zinc Oxide - Synthesis, Methodologies, Reaction Mechanism, and Applications

Sayali Ashok Patil, Pallavi Bhaktapralhad Jagdale, Ashish Singh, Ravindra Vikram Singh, Ziyauddin Khan, Akshaya Kumar Samal and Manav Saxena

The self-archived postprint version of this journal article is available at Linköping University Institutional Repository (DiVA):

<http://urn.kb.se/resolve?urn=urn:nbn:se:liu:diva-191363>

N.B.: When citing this work, cite the original publication.

Patil, S. A., Jagdale, P. B., Singh, A., Singh, R. V., Khan, Z., Samal, A. K., Saxena, M., (2023), 2D Zinc Oxide - Synthesis, Methodologies, Reaction Mechanism, and Applications, *Small*, 19(14), 2206063.
<https://doi.org/10.1002/sml.202206063>

Original publication available at:

<https://doi.org/10.1002/sml.202206063>

Copyright: Wiley

<https://www.wiley.com/en-gb>

Two-dimensional (2D) Zinc oxide – Synthesis, methodologies, reaction mechanism, and applications

Sayali Ashok Patil^{†§}, Pallavi Bhaktapralhad Jagdale^{†§}, Ashish Singh[#], Ravindra Vikram Singh[#], Ziyauddin Khan^{*‡}, Akshaya Kumar Samal^{*§}, Manav Saxena^{*§}

Affiliations:

[§] Centre for Nano and Material Science, Jain University, Ramanagra, Bengaluru, Karnataka-562112, India. *Email:* s.akshaya@jainuniversity.ac.in (AKS) manavsaxena19@gmail.com; s.manav@jainuniversity.ac.in (MS)

[#] R&D Centre, Merck -Living Innovation, Sigma Aldrich Chemicals Pvt Ltd, 12 Bommasandra-Jigani Link Road, Bengaluru, Karnataka-560100, India.

[‡] Laboratory of Organic Electronics, Department of Science and Technology, Linköping University, SE-60174 Norrköping, Sweden. *Email:* ziyauddin.khan@liu.se

Abstract

Zinc oxide (ZnO) is a thermally stable n-type semiconducting material. ZnO 2D nanosheets have mainly gained substantial attention due to their unique properties, such as direct bandgap and strong excitonic binding energy at room temperature. These are widely utilized in piezotronics, energy storage, photodetectors, light-emitting diodes, solar cells, gas sensors, and photocatalysis. Notably, the chemical properties and performances of ZnO nanosheets largely depend on the nano-structuring that could be regulated and controlled through modulating synthetic strategies. Two synthetic approaches, top-down and bottom-up, are mainly employed for preparing ZnO 2D nanomaterials. However, owing to better results in producing defect-free nanostructures, homogenous chemical composition, etc., the bottom-up approach is extensively used compared to the top-down method for preparing ZnO 2D nanosheets. This review presents a comprehensive study on designing and developing 2D ZnO nanomaterials, followed by accenting its potential applications.

To begin with, various synthetic strategies and attributes of ZnO 2D nanosheets are discussed, followed by focusing on methodologies and reaction mechanisms. Then, their deliberation toward , batteries, supercapacitors, electronics/optoelectronics, , photocatalysis, sensing, and piezoelectronic platforms are further discussed. Finally, the challenges and future opportunities are featured based on its current development.

Keywords:

Zinc oxide, 2D nanostructure, Synthesis, Semiconductor, Bottom-up approach, electronics, Energy materials, Catalysis

Table of content:

1. Introduction

2. Synthesis methods

2.1 Ionic layer epitaxy method

2.2 Wet chemical methods

2.2.1 Solvothermal synthesis

2.2.2 Self-assembly-based synthesis

2.2.3 2D-oriented attachment

2.2.4 2D-templated synthesis

2.2.5 Chemical bath deposition

2.3 Other Synthesis Methods

2.4 Physical techniques

2.4.1 Chemical vapor deposition

2.4.2 Atomic layer deposition

2.4.3 Pulsed layer deposition

3. Applications

3.1 Energy storage

3.2 Electronic/optoelectronic devices

3.3 Photocatalysis

3.4 Sensing

3.4.1 Organic compounds

3.4.2 Nitrogen dioxide

3.5 Piezotronics and piezo-phototronics

4. Summary and Perspectives

5. Abbreviation

6. Acknowledgment

7. References

1. Introduction

2D nanostructures and materials have gained widespread attention because of their distinct physical, chemical, optical, and electronic properties compared to the bulk counterpart, which is subjected to the confinement of electrons in two dimensions in the former case. Two-dimensional (2D) nanosheets are a class of 2D nanomaterial consisting of sheet-like structures with lateral sizes ranging from a few nm to hundreds of micrometers [1] and widely being employed in electronic devices, [2-5] catalysis, [6-8] energy storage and conversion, [9, 10] sensing, [11, 12] and biomedicine.[13] In literature, numerous 2D nanostructures such as hexagonal boron nitride (h-BN),[14-17] transition metal dichalcogenides (TMDs), [1, 18-21] graphitic carbon nitride (g-C₃N₄), [22, 23] layered metal oxides, [24, 25] and layered double hydroxides (LDHs), [25, 26] black phosphorus (BP), [27, 28] silicene, [29-31] antimonene, [32-34] have been engineered and subsequently, being utilized for various applications including catalysis, optoelectronics, and energy storage/conversion applications, etc.

The 2D nanostructures are mainly categorized into ‘nonlayered’ and ‘layered’ crystal structures. So far, the exploration of 2D nanostructures has been restricted to naturally layered materials, i.e., van der Waals (vdW) solids with strong in-plane chemical bonds but weak out-of-plane vdW bonds. These 2D layered materials are comprehensively investigated due to the single or few-layer nanosheet, which can be synthesized either by a top-down approach such as mechanical exfoliation, liquid exfoliation, etc., or a bottom-up approach such as chemical vapor deposition, wet chemical synthesis, etc. In definition, the naturally layered materials such as transition metal dichalcogenides, MXenes, black phosphorus, etc. can be easily exfoliated or grown as atomically thin nanosheets due to the strong in-plane chemical bonds but weak out-of-plane van der Waals (vdW) bonds.[35, 36] However, in recent years 2D nanomaterials on nonlayered crystal structures have been reported, such as ZnO, RuO₂, IrO₂, etc [35, 37]. Due

to the inherent isotropic chemical bonds in three dimensions, the synthesis of 2D morphology is not as facile as the case of vdW solids, which requires stabilization of crystal structures far from thermodynamic equilibrium. Also, the typical thickness of these nonlayered 2D materials can be of a few layers of unit cells (0.5 nm to > 10 nm) due to the absence of intrinsic layered configuration. Therefore, 2D nanosheets of nonlayered materials are often called quasi-2D materials. Unlike, 2D layered materials, 2D nonlayered materials possess significant structure distortion with abundant surface dangling bonds and strong chemical bonds in the third dimension, which may provide numerous surface-active sites. Moreover, the exposed surface atom and low coordination numbers stimulate the rate of interfacial charge transfer. Structural and electronic characteristics of non-layered materials can be altered by structure and surface engineering, which offers considerable potential in advanced energy storage and conversion, i.e., batteries, supercapacitors, optoelectronics devices, and sensing. When looking to create 2D nanostructures from non-layered materials, stabilization of crystal structures is essential, which can be achieved by breaking crystal symmetry and inducing 2D anisotropy in crystal growth. [35, 36]

Among various 2D nanostructures, various materials (TMDs, III-IV chalcogenides, metal oxide/hydroxide, etc.) have displayed semiconductor properties. In this context, wurtzite Zinc oxide (ZnO) 2D nanostructures have gained attention owing to having high thermal conductivity (50 W/mK), high surface area, nontoxicity, and being environmentally benign. In addition, a wide direct energy bandgap (3.37 eV) and strong excitonic binding energy (60 meV) at room temperature allow them to be a promising candidate in the realm of photodetectors, light-emitting diodes, gas sensors, solar cells, and photocatalysis.[38-40] In crystallographic terms, the ZnO wurtzite structure is thermodynamically most stable and belongs to a hexagonal unit cell associated with the $P6_3mc$ or C_{6v}^4 space group with $a = b = 0.32539$ nm, and $c =$

0.52098 nm lattice constants and the ratio of c/a is 1.633. The ZnO wurtzite structure is composed of an O^{2-} anion in the corners of the tetrahedron and is stacked with four Zn^{2+} cations in the hexagonal structure along the c axis. ZnO shows dipole moment and polarization along the c axis due to positively charged Zn-(0001) and O-(000 $\bar{1}$) polar surfaces, which are produced by oppositely charged ions due to the difference in surface energy. Wurtzite ZnO structure has anisotropic growth due to (a) different crystallographic planes possessing diverse surface energies and (b) differences in surface polarity and chemical activities.[41] [42]

In the early 2000s, some pioneer work on 2D ZnO nanomaterials using various synthesis strategies which could be scaled up, have been reported. For example, Yu and co-workers had reported the ZnO nanosheet synthesis by oxidizing ZnS nanosheet which possess lateral dimension of 0.3-2 μm with nanometric thin (1.1 nm) nanosheet. First, ethylenediamine passivated ZnS was synthesized at temperature lower than 200 $^{\circ}C$. The role of ethylenediamine is important to maintain the lamellar shape. This nanometric thin ZnO nanosheet are promising candidate in the field of surface related applications.[43] Among various morphologies, ultrawide ZnO nanosheet having exposed large surface area; hence, it is a suitable medium for the development of high-efficiency device.[44, 45] Besides nanosheet-like structures, the self-catalytic and spontaneous formation of two-dimensional web-like structure with tunable dimensions has been reported at low temperatures, indicating its potential application in optical devices.[46] It is proposed that a combination of the "self-catalytic liquid-solid" and "vapor-solid process" mechanism is involved in the synthesis of dendritic nanowires. Hosono and coworkers had reported the synthesis of upright-standing nanocrystalline, porous ZnO film plays crucial role in electronic devices since the vertical intervals facilitate the transport of redox pairs by lowering the cell resistance as well as the recombination of the injected electrons. [47]

By considering advantages of earlier work, chemists and physicists have shown an exciting quest in their respective research fields towards designing and developing 2D ZnO nanosheets because of their exciting properties, as mentioned above. In such a scenario, synthesis approaches become crucial to achieving the desired product. In principle, top-down and bottom approaches are the two synthesis methods that are being used for the synthesis of 2D ZnO nanosheets. In a top-down approach, the bulk counterpart is delaminated or dissociated into 2D nanomaterials. However, issues with the top-down method are associated with low yield, smaller lateral sizes with defects, aggregation, and poor stability. At the same time, the bottom-up approaches have gained much attention and are being utilized to synthesize ZnO 2D nanostructures. The bottom-up approach consists of a wide range of methods, e.g., templated synthesis by assembling atoms, and molecules through chemical vapor deposition (CVD)[48-55] and wet-chemical synthesis methods.[56-63] Importantly, the *bottom-up approach* also offers control over the growth of morphology and structure of desired materials [64] and, therefore, could pave the way to overcome the limitations of the top-down approach. However, a considerable lacuna exists in explaining the systematic progress and development of the synthesis and applications of 2D ZnO nanosheets.[65-67] The existing reviews on ZnO nanomaterials focus on and discuss the mixed synthesis of 0D-3D nanostructures and applications.[65-67] To the best of our knowledge, a comprehensive overview focused on synthesizing 2D ZnO nanosheets and their applications have yet to be reported. Thus, *there is plenty of room for compiling a systematic evolution discussing the fundamental & mechanistic aspects of synthesis and applications of 2D ZnO nanosheets.*

Based on the kinds of literature, it can be found that 2D ZnO nanosheet has unique physiochemical, electronic, and optical properties compared to the other dimensions benefiting potential applications. For example, electron confinement of 2D ZnO nanosheets in nanometric

regions advances their electronic characteristics, which is beneficial for optoelectronics devices.[68] Further, strong in-plane stability and ultrathin thickness boost the mechanical properties, flexibility, and optical transparency of the 2D ZnO nanosheet, which is favorable for device fabrication.[69] The large surface area of 2D ZnO nanosheet provides more exposed surface atoms, which is a promising feature for surface-related applications such as sensing,[70] [71] catalysis,[72] [73] and energy storage devices. [74] [75]

This review briefly overviews the various synthetic approaches utilized to synthesize 2D ZnO semiconductor nanosheets (Figure 1). The synthesis section discusses the chemical reactions, mechanism, and reaction parameters. Afterward, the potential applications of 2D ZnO nanosheets in electronics/ optoelectronics, electro/photocatalysis, batteries, supercapacitors, solar cells, and sensing platforms are also summarized and discussed (Figure 1).



Figure 1. Schematic illustration of synthesis strategies and applications of ultrathin 2D ZnO.

Table 1: Literature on 2D ZnO nanomaterials synthesis.

S. No.	Method	Film Morphology	lateral size (μm)	Thickness (nm)	Application	Ref
1	Ionic layer epitaxy	Triangular	0.02	2.3	Optoelectronics	[68]
2	Ionic layer epitaxy	Triangular	10	1.8 ± 0.2	-	[76]
3	Hydrothermal	Hexagonal	3.6	10	Solar cell	[77]
4	Solvothermal	Hexagonal	1-1.5	50-200	-	[78]
5	Solvothermal	-	1-10	3.35	Photodetector	[79]
6	Hydrothermal	Hexagonal	3.5-7.6	40	Ethanol sensing	[80]
7	Solvothermal	Rectangular	Several hundred nm	10-30	Photocatalytic	[72]
8	Hydrothermal	-	-	50	Batteries	[74]
9	Solvothermal	Sheet	-	13.5	Acetone sensing	[81]
10	Self-assembly	Hexagonal	0.025	-	acetaldehyde sensing	[82]
11	Self-assembly	Thin layer	10	1	-	[83]
12	Self-assembly	Irregular	0.3-1	50	H ₂ sensing	[70]
13	2D template	-	20	0.28	-	[84]
14	2D template	Hexagonal	-	2.9	Acetylacetone sensing	[85]
15	Chemical vapor deposition	-	tens of μm	50	Acetone sensing	[86]
16	Chemical bath deposition	-	few microns	<50	Batteries	[75]
17	Oxidation	Thin layer	several μm	2	-	[87]

18	Calcination	Thin layer	tens of μm	15	Batteries	[88]
19	Electrodeposition	Hexagonal	1.2	30-50	Photocatalytic	[89]
20	CVD	Irregular	5-10	11.9	Optoelectronics	[69]
21	Ultrasonic assisted	Hexagonal	0.01	30	Photocatalytic	[90]
22	Hydrothermal	-	5	100	Ethanol sensing	[91]
23	Hydrothermal	-	3-6	10-40	Ethanol sensing	[92]
24	Microwave synthesis	-	<0.9	40-80	NO_2 sensing	[93]
25	solution methods	-	1	80	NO_2 sensing	[94]
26	solution methods	-	0.2-0.5	20	NO_2 sensing	[95]
27	Ionic layer epitaxy	Triangular	10-40	2-3	Piezotronics	[96]
28	Ionic layer epitaxy	Triangular	0.5	0.5	Piezotronics	[97]
29	Solution methods	-	4.2-2.4	-	Piezotronics (nanogenerators)	[98]
30.	Hydrothermal	-	-	45 \pm 5	H_2 sensing	[99]
31.	Calcination	Rectangular	0.8	6-7	CO_2 reduction	[100]
32	Hydrothermal	-	3	-	Photocatalytic	[101]
33	Hydrothermal	Nanonet	1	25	Organic amines sensing	[102]
34	Electrochemical deposition	Hexagonal	1.14-1.66	16-67	Solid phase microextraction	[103]
35	Chemical bath deposition	Sheet	-	18-22	Humidity sensor & photodetector	[104]
36	Sonochemical	Sheet	2-5	8	photocatalysis	[105]

2. Synthesis strategies

To explore the properties, functions, and applications, it is imperative to develop facile, feasible, controllable, and reliable methods for preparing 2D ZnO nanomaterials. In contrast to top-down approaches, as discussed above, a bottom-up synthesis entails chemical reactions occurring at optimized parameters and controlled precursor concentration. Strategies based on bottom-up synthesis are generally more adaptable to yield defect-free 2D ZnO nanosheets, which might open up the possibility of exploring unforeseen properties of ZnO. Specifically, some of the well-established bottom-up synthesis approaches used in the fabrication of 2D ZnO nanostructures are summarized in this section. *Further, we also discuss the chemical reactions, reaction mechanisms, and the effect of reaction parameters in the synthesis.*

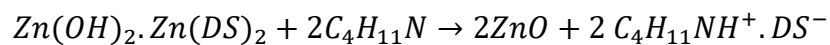
2.1 Ionic layer epitaxy (ILE):

The ultrathin, 2D free-standing nanostructure is a new class of advanced functional materials which open up exclusive properties of nanomaterials with thin-film mechanics into confined 2D space.[106] These soft mechanics assist their controllable folding and free-standing systems, which can expose both ends to the environment.[107] Surfactants (amphiphilic molecules) could be used as a template to grow the 2D nanomaterials and to control the nanomaterials' morphology.[108] The surfactant is known to be selectively adsorbed onto certain crystallographic facets to give anisotropic growth.[109, 110]

In recent years, ionic layer epitaxy (ILE) has been developed to grow nanometer-thick with the size of tens of micrometer nanosheets using aqueous solutions.[111] Wang and co-worker produced surfactant-assisted large-area zinc hydroxide dodecyl sulfate (ZHDS) film at the water-air interface via ionic layer epitaxy (ILE) using amphiphilic surfactant as a soft

template.[108] In a reaction, an aqueous solution of zinc nitrate hexahydrate and hexamethylenetetramine (HMTA) as a precursor along with sodium dodecyl sulfate (SDS) (above critical micelle concentration) was kept at 90 °C for 4 h in a conventional oven which leads the formation of continuous membrane on the water. TEM study suggests that the overlapping of individual hexagonal grains leads to the formation of continuous nanosheets having a single layer thickness of 4 nm (Figure 2 a-b). The hexagonal helical contours on the surface are due to screw dislocation (Figure 2 c). Figure 2 d illustrates the plausible formation mechanism of the ZHDS membrane at the water surface. The negatively charged dodecyl sulfate ions (DS ions) form a monolayer at the water-air interface, and the Zn^{2+} ions form an electric double layer. At 60 °C, HMTA decomposes into ammonia and formaldehyde, which initiate the crystallization of ZHDS to form a stern layer. Further, it is observed by the same group that the reaction time also plays a crucial role in tuning the morphology. For instance, the phase transformation exhibited by increasing the reaction time to 20 h, followed by forming rectangular sheet-like morphology. [112] Figure 2 e displays an optical microscopy image of the rectangular sheet on a 100 nm SiO_2/Si substrate. This suggests that the ZnO sheets have lateral sizes of 50-100 μm in breadth and 100-300 μm in length. Notably, the sheet shows two types of morphology as confirmed by AFM topology scan, i.e., flat surface with thickness 108 nm (Figure 2 f) and hillocks pyramid-like structure with step thickness of 10-120 nm in range (Figure 2 g). Further, the TEM image suggests the rectangular morphology of the sheet (Figure 2 h). The corresponding SAED pattern shows hexagonal symmetry (bright spots) and orthorhombic superlattice (weak spots) (inset Figure 2 h). Hexagonal symmetry is due to the crystal structure of ZHDS. At the same time, an orthorhombic superlattice formed because of the long-range order of zinc vacancies recognized by orthorhombic spots.[113] A time-dependent nanosheet evolution experiment had carried out to investigate the formation of the rectangular phase from the hexagonal phase by collecting nanosheets from the water-air

interface at different reaction intervals. The phase transformation occurs due to the precursor diffusion at the water surface, leading to zinc vacancies forming. The phase transformation mechanism is likely to be completed in three steps: (i) *Reaction-limited growth*: initially, a hexagonal nanosheet formed on the water surface supported by a thin surfactant layer. Zn^{2+} ions can easily diffuse towards the growth site, and the hexagonal sheet proliferates (ii) *Diffusion limited stage*: As reaction time increases sheet grows thicker and thicker, which limits the diffusion of Zn^{2+} ions. (iii) *Completion of phase transformation*: Due to the lack of Zn^{2+} ions, the formation of zinc vacancies takes place, followed by a periodic slip process and, finally, a hexagonal phase transfer into a rectangular phase (Figure 2 h). The intercalated or surface termination plays a crucial role in the electrical and mechanical properties of the materials. Thus, removal of intercalated DS^- ions in between the ZnO sheets were removed using n-butylamine to improve the electrical and mechanical properties of the ZnO sheets. Upon addition of n-butylamine to the ZHDS sheet solution, the DS^- ions are easily removed due to electrostatic forces, and pure ZnO sheets are formed. The hydroxyl (-OH) groups in the ZHDS sheet are highly polarized. The H atom tends to form a bond with oxygen on the sulphate group, form dodecyl sulfuric acid, and later react with n-butylamine by the acid-base reaction. Otherwise, it could first be attached with n-butylamine and form a cationic surfactant that combines with DS ions. In both, the reaction n-butylammonium dodecyl sulfate salt was a by-product. The chemical reaction of the process is as follows:



The TEM image of exfoliated ZnO nanosheets displays a ribbon-like rolled-up structure due to the surface strain on pure ZnO nanosheets. HRTEM image shows the polycrystalline nature of the nanosheet (Figure 2 i). The folded ZnO nanosheet confirms the flexibility as observed by SEM analysis.

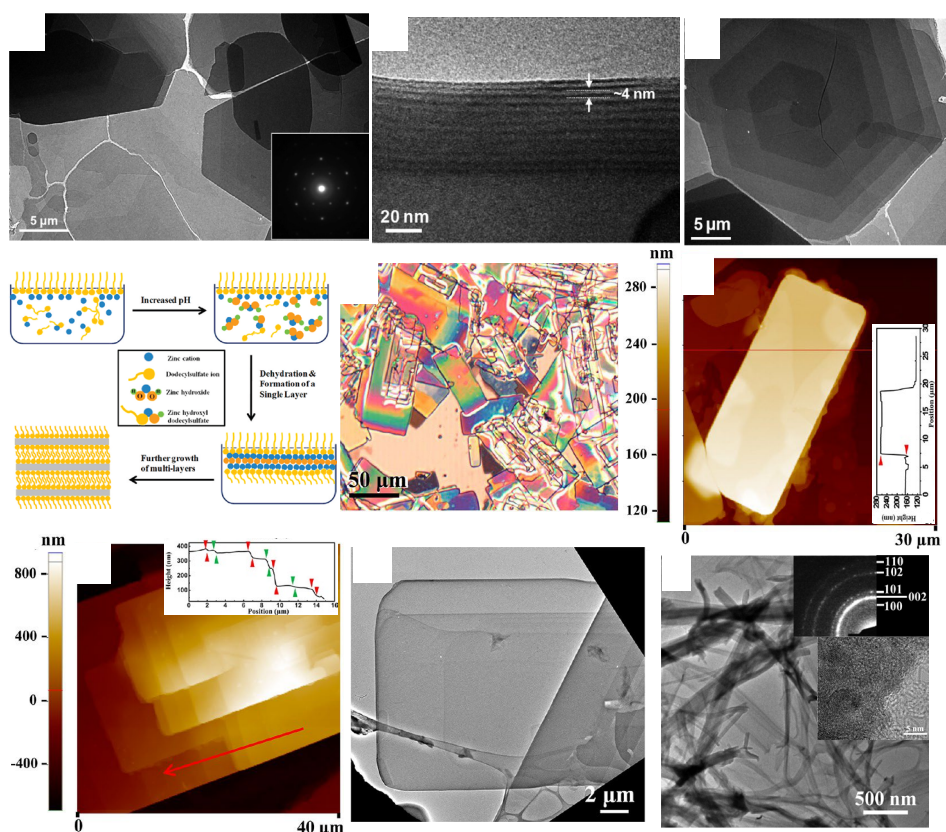


Figure 2. (a-c) TEM image of ZHDS nanomembranes. (a) TEM image at low magnification, inset: electron diffraction pattern of a single grain. (b) Cross-sectional TEM image of ZHDS nanomembrane, (c) Hillock pyramid-like the hexagonal surface of a single grain. (d) Schematic illustration of evaluation of ZHDS nanomembrane at the water-air interface. “Reprinted from permission [108]. Copyright 2012, American Chemical Society”. (e-i) rectangular ZHDS sheets (e) Optical image, (f-g) AFM scan topographical images of flat-surfaced rectangular sheet and spiral growth rectangular sheet respectively with line profiles, (h) TEM image of single rectangular ZHDS sheet with electron diffraction pattern (inset), (i) TEM image of the exfoliated sheet, inset: HRTEM image and corresponding electron diffraction pattern. “Reprinted from permission [112]. Copyright 2013, American Chemical Society.”

In another ILE approach, Wang and co-workers have synthesized a single crystalline ZnO nanosheet using oleyl sulphate as a precursor. [68] In a typical synthesis, sodium oleyl sulfate (0.1 vol % in CHCl_3) was spread over the surface of the nutrient solution (metal ion solution), followed by heating at 60 °C for 100 min. Anionic oleyl sulfate forms a closely packed monolayer at the water-air interface, and Zn^{2+} cation is attracted to form an electric double layer (Figure 3 a). Densely packed triangular ZnO nanosheets are 2.28 nm thick with a lateral size of ~20 nm (Figure 3 b, c). The single crystalline nature of the nanosheet is confirmed by HRTEM analysis. The selected area electron diffraction (SAED) pattern shows 2.81 Å lattice spacing which corresponds to the wurtzite (0001). The overlayer growth on nanosheets indicates the layer-by-layer growth mechanism (Figure 3 d). Based on the time-dependent study, it was confirmed that initially formed amorphous film upon aging gives rise to random crystallite, and that was further rearranged in the same hexagonal crystal plane to yield a single-crystalline nanosheet (Figure 3 e). The further study explored the effect of precursor concentration, surfactant, and reaction time on the lateral size and thickness of the ZnO nanosheet. [114] The precursor and surfactant concentration could alter the kinetics of the reaction, thickness, and lateral size. The denser the anionic monolayer more Zn^{2+} cations would attract to form an electric double layer.

Further, Yin and co-workers investigated the influence of surfactant packing density on the nanosheet's lateral size and thickness. They synthesized ZnO nanosheets at different surface pressure using the ILE method in the trough reactor by controlling the surfactant spreading area at the water surface.[115] The surface morphology of the synthesized nanosheet at different surface pressure was characterized using FE-SEM (Figure 3 f). The nanosheets are ~2.35 nm thick at 16.38 mN/m surface pressure, as shown in Figure 3 g. Wrinkles on the nanosheet in the TEM image indicate excellent flexibility of the nanosheet. HRTEM confirms the single

crystalline structure with the hexagonal arrangement (Figure 3 h). SAED pattern shows wurtzite crystal structure with (0001) plane and $\{10\bar{1}0\}$ [28] (inset Figure 3 h). Further, the thickness of the nanosheet increases with surface pressure, as confirmed by the AFM study. At the low surface pressure, surfactant molecules were randomly oriented, producing a weak electric field due to the low charge density. Consequently, less amount of zinc ions was attracted towards the surfactant layer resulting in a thinner sheet. With the increase in the surface pressure, the surfactant molecules became closely packed and formed a strong electric field between the surfactant layer and beneath Zn ions. Consequently, the large numbers of Zn ions attracted towards the surfactant layer to form a thicker nanosheet. Further increase in surface pressure enhances the repulsive force between two molecules, which causes wrinkles and irregular surfactant packing. At this stage, the nucleation density of Zn^{2+} ion and surfactant density are the governing factors at low and high surface pressure that influence the growth of nanosheets. As a result, polycrystalline ZnO nanosheets, which possess strong ferromagnetism, couldn't be prepared by the ILE method at the water-air interface.[76] In this direction, Yin and co-workers prepared polycrystalline triangular ZnO nanosheets by the ILE method at the water-oil interface. In place of surfactant as per Wang's procedure[68], the organic solvent (toluene, hexane, or cyclohexane) was spread on the surface of the nutrient solution and heated at 60 °C for 105 min, which resulted in densely packed equilateral triangular nanosheets with $\sim 2\text{-}10\text{ }\mu\text{m}$ lateral sizes with $\sim 1.8 \pm 0.2\text{ nm}$ thickness (Figure 3 i, j). HRTEM images exhibit polycrystalline nature with $\sim 10\text{ nm}$ average size irregular crystalline domains (Figure 3 k). The polycrystallinity of the ZnO nanosheet is confirmed by the SAED pattern, which was further supported by the FFT pattern and confirmed hexagonal wurtzite structure (inset Figure 3 k). The effect of the oil phase on the structure and morphology of ZnO nanosheets was compared by synthesizing ZnO nanosheets at water-oil and water-air interfaces. The nanosheets synthesized at water-oil interfaces are thinner than those synthesized at water-air interfaces.

Molecular dynamics (MD) simulations were carried out to understand the effect of interfaces mechanistically during nanosheet growth and thickness. The surfactant monolayer formed at the water-oil interface demonstrated higher roughness than the water-air interface at the same surfactant density and Zn^{2+} ion concentration. In water-oil interfaces, surfactants are dragged more toward the oil phase; hence, small-sized nanosheets were formed at the water-oil interface. However, at constant surfactant concentrations, the charge distribution perpendicular to the water surface became wider than the water-air interface. Hence, the total charge distribution in both cases was the same, but charge density was lower at the same depth from the interface in the water-oil as compared to the water-air interface. The lower charge density results in a thin stern layer of Zn^{2+} ions at the water-oil interface forming an ultrathin nanosheet.

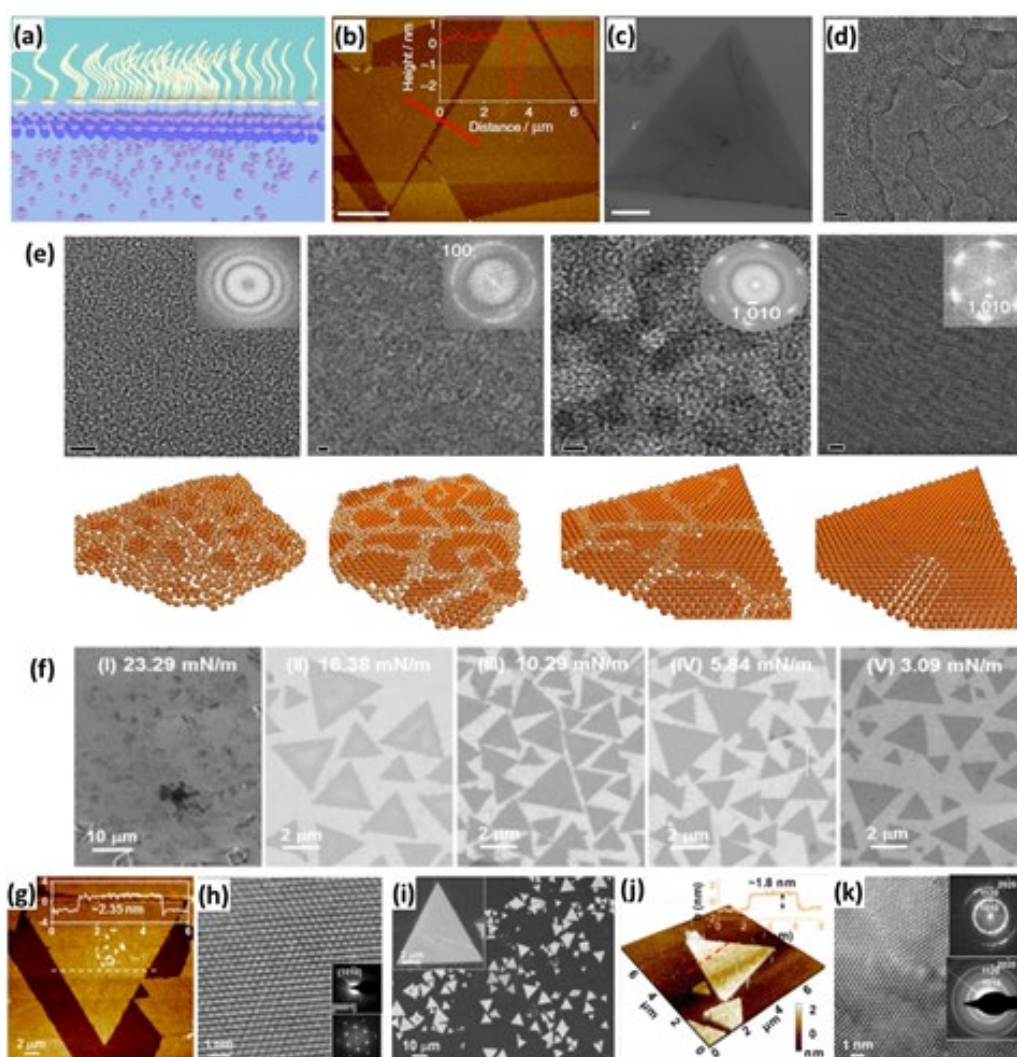


Figure 3. (a) Schematic representation of the formation of ZnO nanosheet at the water-air interface, (b) AFM topography scan (scale bar 5 μ m), (c) SEM image of individual ZnO nanosheet (scale bar 5 μ m), (d) HRTEM image shows overgrowth of nanosheet (Scale bar 2 nm), (e) Schematic representation of time-dependent evolution of ZnO nanosheet. “Reprinted from permission [68]. Copyright 2016, Nature Communications.” (f) SEM image of ZnO nanosheet at different surface pressure, (g) AFM image of ZnO nanosheet with height profile, (h) HRTEM image shows wurtzite lattice structure with Fast Fourier Transform FFT pattern (lower inset) and electron diffraction pattern, (upper inset). "Reprinted from permission [115]. Copyright 2017, American Chemical Society.” (i) Large area SEM image of ZnO nanosheet (inset magnified image), (j) 3D nanosheet with height profile (inset image), (k) HRTEM image of wurtzite ZnO with inset SAED (right top) and FFT (right bottom) pattern of ZnO nanosheet which confirms polycrystalline nature of nanosheet. "Reprinted from permission [76]. Copyright 2017, American Chemical Society.”

Crystal growth to produce crystalline nanomaterials must abide by the crystal growth theory. [116, 117] Due to their specific adsorption on crystallographic facets, the surfactants utilized in the synthesis confine/decelerate crystal development, which initiates 2D growth. The screw dislocation growth is a fundamental crystal growth mechanism that exists in various materials and supersaturation regimes. This phenomenon is mainly observed at low supersaturation, where the mechanism of layer-by-layer growth and dendrite growth is suppressed. Screw dislocation growth provides a self-perpetuating step edge that grows in a spiral trajectory around the burger vector. Morin and co-workers reported the screw dislocations driven growth of zinc hydroxyl sulfate, ZHS [3Zn(OH)₂.ZnSO₄.0.5H₂O] nanoplates using, ZnSO₄, Zn(NO₃)₂, and HMTA as precursors over a wide range of temperatures (60-95 °C).[118] A morphology

study of ZHS nanoplates revealed that hexagonal nanoplates are densely packed (Figure 4 a-c) and have polycrystalline nature (Figure 4 d). The lateral growth velocity at the steps on the dislocation hillocks explains the screw dislocation-directed 2D spiral growth motion and surface hillocks formation process (Figure 4 e). The lateral growth velocity of outer edges and steps decide the formation of rod/screw dislocation or 2D sheets. The authors also synthesized and explained screw dislocation-driven growth for other transition metal hydroxides.

In further research, Wang and co-workers wisely took advantage of the mixed surfactant to synthesize monocrystalline 2D nanosheet using ILE.[119] In this process, the optimized ratio of the opposite surface charges regulates the ions aggregation by controlling nucleation and directing the growth of inorganic crystals to give a large area of monocrystalline nanosheet. An aqueous solution of zinc and nickel salts in the typical synthesis with HMTA was prepared in the optimized ratio. An appropriate molar ratio of Sodium oleyl sulfate (SOS), anionic, and oleyl amine (OAM) cationic surfactant solution in chloroform was spread on the surface of the precursor solution to get the film at the water-air interface at 60 °C. In the growth process, negatively charged SOS surfactant produced a continuous film of Ni-doped ZnO at the water-air interface (Figure 4 f). However, after mixing positive OAM surfactant, pores were developed in a continuous film, and finally, a single-layer triangular/hexagonal nanosheet was formed. However, upon OAM addition, a stable, single layer, 2 nm thick triangular nanosheet was formed (Figure 4 g-h). The d-spacing of 0.281 nm and the corresponding SAED pattern (Figure 4 i) suggested the single crystalline wurtzite structure.

The ILE method is mainly used to synthesize controllable growth of defect-free ultrathin, large-area nanosheets offering improved interfaces for heterostructure devices. Ultrathin features of the nanosheet tuned the nanosheet's optical, mechanical, electronic, and magnetic properties, which is beneficial for the reliability of device efficiency and heterostructure device formation.

The free-standing assembly provides easy transferring of the nanosheet, diminishing substrate effect, and flexibility of the nanosheet. In addition, for the synthesis of large area nanosheets, different templates are used. Removal of the template causes detrimental consequences on the morphology of the nanosheet. In ILE, surfactant molecules are widely used as soft templates to grow the nanosheet which can be easily removed without damaging the nanosheet.

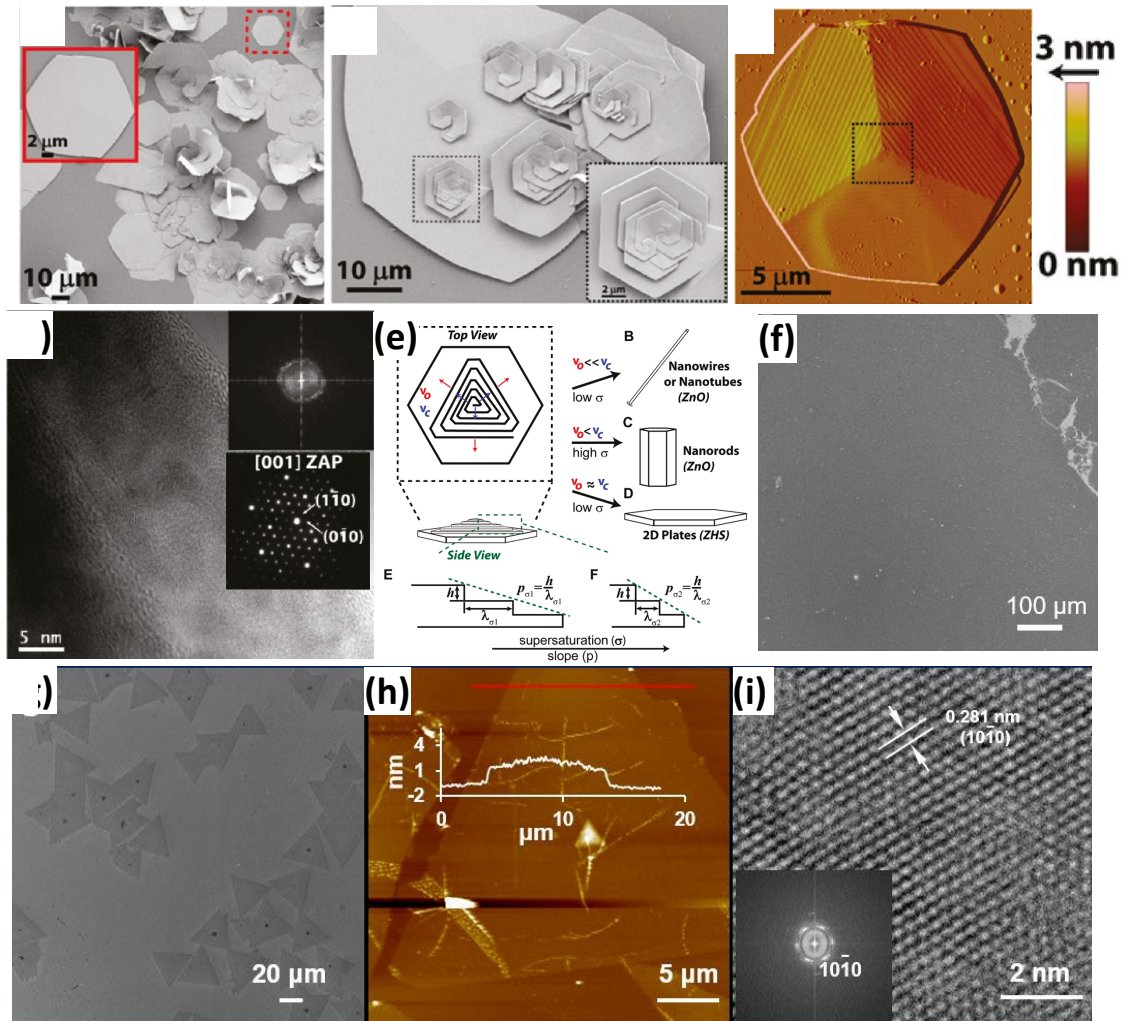


Figure 4. (a-b) SEM image of an as-synthesized flat surface, (b) Hillock hexagonal nanoplates, (c) AFM topography scan of dislocation core, (d) High magnification TEM image of ZHS with inset SAED and FFT pattern respectively, (e) Schematic representation of dislocation-driven growth of different nanomaterials. “Reprinted from permission [118]. Copyright 2011,

American Chemical Society.” (f-g) SEM images, (h) AFM images, and (i) HRTEM images inset: SAED pattern of ultrathin Ni-doped ZnO nanosheet with SOS. “Reprinted from permission [119]. Copyright 2019, American Chemical Society.”

2.2. Wet Chemical Method:

Next, wet chemical synthesis is another promising method for preparing ultrathin 2D nanomaterials [56, 57] which involves chemical reactions between precursors under optimized experimental conditions.[120] The high solution processability, controllability, and good yield are the positive aspects of the wet chemical method for large-scale applications.[1] The wet chemical method is categorized further into solvothermal synthesis, 2D-oriented attachment, 2D-templated synthesis, self-assembly of nanocrystals, interface-mediated synthesis, and on-surface synthesis, which all are discussed separately.

2.2.1. Solvothermal Method:

In the solvothermal method, the concentration of the precursor(s), solvent system, surfactants or polymers, and reaction temperature are the crucial parameters that affect the product's morphology and chemical and physical properties. Jung and co-workers reported single-crystalline ZnO morphologies using various surfactants.[77] Different surfactants interact differently with the precursors, yielding various nanostructures for the ZnO 2D sheet. For instance, the hexagonal ZnO nanosheet was synthesized using an equimolar concentration of zinc nitrate hexahydrate, HMTA, and sodium dodecyl sulfate (SDS), at 90 °C for 24 h. The collected product was further annealed at 350 °C for 1 h to eliminate organic residues from the product. SDS tail possesses a negatively charged sulfonic acid group attached to the Zn^{2+} terminal (0001) plane to suppress material growth along the c-axis due to the strong charge

interaction. Consequently, a stable, thin hexagonal nanosheet was formed along the $(10\bar{1}0)$ growth direction. Unstacked hexagonal nanosheets with a lateral size of $\sim 3.6 \mu\text{m}$ (Figure 5 a) and thickness of 10 nm (Figure 5 b) were observed due to the electrostatic repulsion between nanosheets which was aroused from similar hydrated ions (Na^+) present in surfactant. HRTEM image revealed that the ZnO nanosheets were building up by an assembly of 10-20 nm hexagonal ZnO nanoparticles (Figure 5 c). To understand the morphology effect of the anion, another surfactant with the same length of the alkaline chain but different counter ions have used in place of SDS. The results indicate that cationic counter ions tune the ZnO morphology, such as shape and nanosheet thickness. This is attributed to larger hydrated ions due to the strong interaction with water molecules. The DS anion present on the (0001) plane of the Zn^{2+} end suppressed the growth of the nanosheet along the c-axis.

Further, Zhang and co-workers demonstrated another solvothermal method for preparing a ZnO disk using sodium dodecylbenzene sulfonate (SDBS) and a zinc precursor in ethanol/water solvent.[78] The solvothermal process was conducted at 90°C for 4 h followed by heating at 180°C for 4 h. FESEM image confirms the crystalline hexagonal-shaped ZnO disks supported by smooth edges (Figure 5 d-e). The d-spacing of 0.28 nm corresponds to $[000\bar{1}]$ plane of the wurtzite crystal structure observed (Figure 5 f). The role of anionic surfactant, sodium hydroxide, and reaction temperature on the morphology of ZnO disks help to conclude that (i) the thickness of the disks decreases with an increase in surfactant concentration, (ii) larger plates and bilayer hexagonal disks were obtained at low and high concentrations of NaOH, respectively, (iii) reaction temperature supports fast growth of ZnO disks, (iv) in fix concentration of SDBS and Zn^{2+} , the number of water influences the morphology.

Further, Sun and co-workers reported the preparation of ZnO nanosheet via solvothermal method using amphiphilic block copolymer surfactant and ethylene glycol (EG) as a structure-directing agent, which helps stacking and growth of 3.35 nm thin crystalline ZnO sheet with wurtzite structure.[79] Surface morphology analysis confirms a large area sheet with a rolled edge which might be due to the surface tension (Figure 5 g). HRTEM demonstrated the ZnO sheet's highly crystalline wurtzite structure (Figure 5 h). Importantly, EG plays a crucial role in the formation of inverse micelles which separate the lamellar phase and form a more stable lamellar structure.

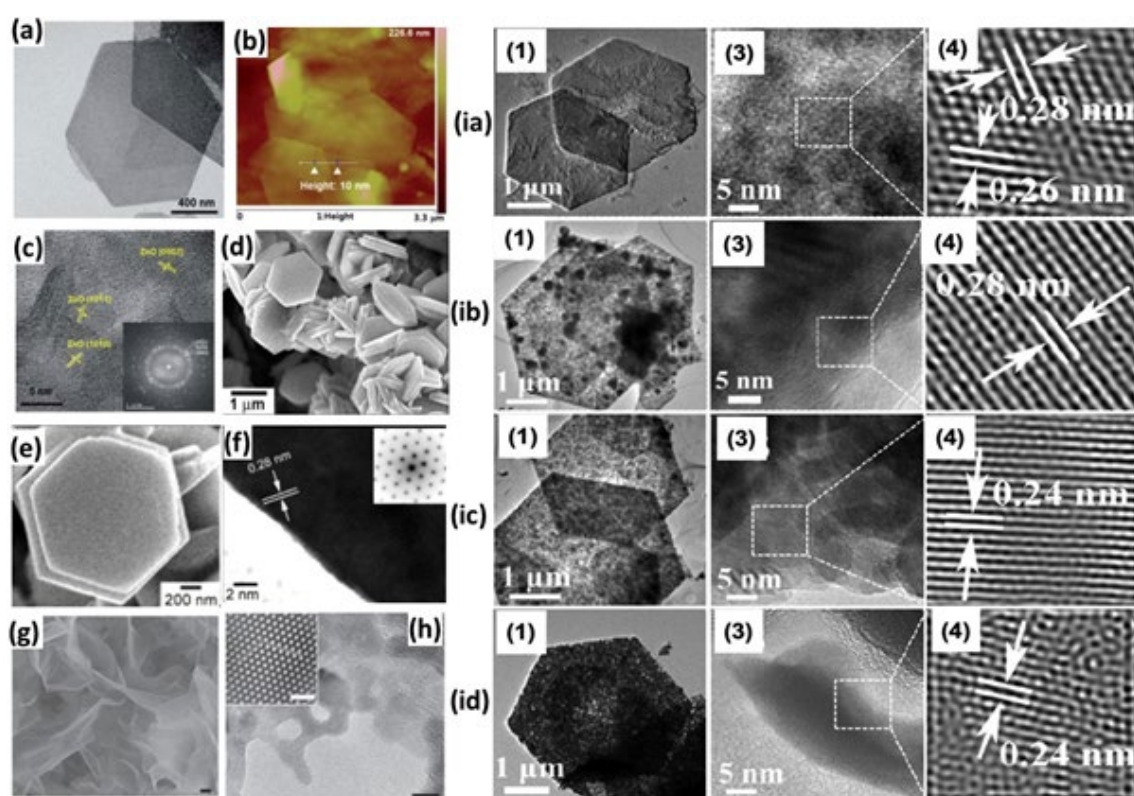


Figure 5. (a) TEM image, (b) AFM image, (c) HRTEM image with SAED pattern (inset) of ZnO nanosheet. “Reprinted from permission [77]. Copyright 2014, Royal Society of Chemistry.” (d) Low magnification, (e) Higher magnification SEM image of as-synthesized bilayer hexagonal ZnO disks, (f) HRTEM image and SAED pattern (inset) of ZnO disks. “Reprinted from permission [78]. Copyright 2009, American Chemical Society.”(g) SEM

image of ZnO nanosheet (scale bar 200 nm) (h) HRTEM image of ZnO nanosheet (scale bar 5 nm) and inset: HRTEM images of the crystal lattice structure of the nanosheets (scale bar 1 nm). "Reprinted from permission [79]. Copyright 2014, Nature Research." (i) TEM and HRTEM image of (a) $\text{Zn}_5(\text{OH})_8\text{Cl}_2\text{H}_2\text{O}$, (b) ZnO-300, (c) ZnO-500, (d) ZnO-700. "Reprinted from permission [80]. Copyright 2017, Elsevier."

Further, Zhang and co-workers prepared hexagonal ZnO nanosheets via the facial hydrothermal method.[80] In a typical synthesis, zinc chloride (ZnCl_2), urea, and polyvinylpyrrolidone (PVP) polymer were added into ethanol/water mixed solvent. Hydrothermal synthesis was carried out at 90 °C for 24 h. As synthesized ZnO nanosheet was annealed at a different temperature to produce a porous ZnO nanosheet. The lateral size and thickness of the as-synthesized $\text{Zn}_5(\text{OH})_8\text{Cl}_2\cdot\text{H}_2\text{O}$ sheet lies between 3.5-7.6 μm and ca. 40 nm. After annealing at a different temperature, porous ZnO sheets were formed, as shown in Figure 5 i. Synthesized ZnO nanosheet was further studied for gas sensing, described later in the review.

Liu and co-workers reported template, surfactant, and polymer-free synthesis of porous ZnO nanosheets with a regular rectangular morphology by solvothermal method followed by annealing for 2 h in the air at different temperatures up to 700 °C.[72] As the annealing temperature increases, the crystallite size of the ZnO particles moderately increases, and the morphology of the sample breaks and rebuilds the surfaces. HRTEM image of ZnO-300 °C confirmed single-crystalline wurtzite nature with d spacing 0.514, 0.277, and 0.246 nm indexed to $\{0002\}$, $\{10\bar{1}1\}$, and $\{10\bar{1}0\}$ planes, respectively. HRTEM and FFT patterns suggest that the nanosheet growth is parallel to $[0001]$ crystallographic direction (c axis) and perpendicular to $[01\bar{1}0]$ plane. As the annealing temperature increased to 500 °C, fewer clear fringes with some disordered areas were observed. Consequently, defects were formed in the ZnO

nanosheet. Further, increasing the annealed temperature of the ZnO nanosheet to 700 °C, the HRTEM image indicated 0.281 nm d-spacing indexed to $\{10\bar{1}1\}$ planes with ordered area leading to reduce the defect in the ZnO nanosheet.

2.2.2. Self-assembly method:

Self-assembly of low-dimensional nanocrystals (nanoparticles, nanowires) has emerged as a promising way to prepare ultra-thin 2D nanostructures. Nanocrystals prepared through this technique are assembled by non-covalent interactions like van der Waals, electrostatic interactions, and hydrogen bonds.[121] However, these 2D structures are not continuous. As a typical example, Du and co-workers prepared hexagonal grid-like ZnO lamellae (GZL) by the o-phthalic acid-assisted hydrothermal method followed by calcination.[82] The side-by-side linkage of the nanoparticles is confirmed using cross-sectional SEM. HRTEM image showed ZnO lamellae made up of an assembly of hexagonal nano tablet with a diagonal length of ~25 nm and edge length of ~12 nm. Lattice distance (d) of 0.238 nm was observed, corresponding to the (100) plane of the wurtzite hexagonal structure of ZnO. Notably, the o-phthalic acid plays a vital role in tuning the morphology from ZnO nanoparticles to hexagonal shape.

Hou and co-workers have reported an exciting self-assembly method, reagent-free electrophoretic synthesis of free-standing nanometric polycrystalline ZnO nanosheets from ZnO quantum dots (QDs).[83] Anodic Zn precursor and cathodic graphene paper were dipped into the Milli Q water. After applying the electric field, the water's electrolysis occurs; consequently, ZnO QDs were generated from anode material. The prepared QDs uniformly assembled on the cathode. The SEM image shows the free-standing ZnO nanosheet with several nanometer lateral sizes (Figure 6 a). Inset element mapping confirms that the Zn and O elements are uniformly distributed, and the thickness of the ZnO nanosheet is less than that compared to the carbon film. Height profile measurement (inset, Figure 6 b) shows 1nm

thickness of the single-layer ZnO nanosheets and 2 nm thickness of bilayer folded nanosheets. HRTEM image, SAED pattern, and Fast Fourier transform (FFT) suggested the free-standing, folded polycrystalline ZnO nanosheets with hexagonal wurtzite structure. (Figure 6 c-f). Based on TEM analysis, it was concluded that the surface of the ZnO nanosheet was dominated due to the (002) planes. Further, the orientation of the c-axis of the ZnO crystal perpendicular to the plane sheet was reduced, indicating that the nanosheet's thickness is twice that of the unit cell on the c-axis of ZnO. Based on the experimental results, the synthesis mechanism of the 2D nanosheet by assembly could be explained in three steps: (i) oxidation of Zn anode and hydrolysis reactions produce 1 nm thick and ~4 nm diameter ZnO QDs. During the synthesis of ZnO QDs, the pH of the solution around the anode was decreased. Due to low pH, protons from the environment shifted toward the ZnO QDs surface, subsequently forming the Zn-OH_2^+ surface group. (ii) ZnO QDs assembled and formed 2D nanoribbons with 1 nm thickness. During the assembly of ZnO QDs, polar facets were dominated on the nanostructure surface resulting in a reduction at the nonpolar facet. (iii) Moreover, ZnO nanoribbons are assembled to form 1 nm-thick nanosheet mainly situated near the cathode area. The electrostatic repulsion between the nanosheets gradually increases due to the increase in charged surfaces, and consequently, the ZnO nanosheet is in a colloidal suspension.

2.2.3. 2D-oriented attachment:

In an oriented attachment mechanism, nanometer-sized adjacent particles align by sharing the same crystallographic orientation, forming a single-layer crystalline 2D nanosheet without increasing the sheet thickness.[122-124] Oriented attachment results in a controlled growth process and produces nanocrystals with well-defined morphology.[57, 125, 126] Sahu and co-workers prepared ZnO nanosheets by oriented attachment of ZnO nanoparticles synthesized using different zinc precursors.[127] AFM topology scan reveals that anions play a crucial role

in the lateral size and thickness. The thickness of nanosheets was observed to follow an order: CH_3COO^- (23 nm) > NO_3^- (13 nm) > SO_4^{2-} (9.5 nm) based on counter anion in the Zn-precursor. The result confirmed that the counterions of the precursor influence the size and thickness of the ZnO nanosheet. The two-step growth mechanism of ZnO nanosheets was studied (i) nucleation and growth of nanoparticles of ZnO, and (ii) formation of ZnO nanosheet using oriented attachment of the self-assembling ZnO nanoparticles. *In the first step*, when OH^- ions were appended into a Zn^{2+} aqueous solution with different counter anions, nanosized $\text{Zn}(\text{OH})_2$ precipitates and $[\text{Zn}(\text{OH})_4]^{2-}$ were formed. The formation growth of $[\text{Zn}(\text{OH})_4]^{2-}$ is caused by excess OH^- ions in the solution. Upon heating, precipitated nanosized $\text{Zn}(\text{OH})_2$ were reduced to form ZnO nanoparticles. *In the second step*, synthesized ZnO nanoparticles dispersed in the reaction solution and self-assembled moiety go through the oriented attachment mechanism to form ZnO nanosheets. Significantly, the interaction between OH^- ions with Zn^{2+} ions impacts the adsorption of counter ions onto $\text{Zn}(\text{OH})_2$ precipitate. As a result, the ZnO nanosheet growth rate was influenced because of the different polarities of counter ions. In another study, Wang and co-workers reported the synthesis of porous ZnO nanosheet by heating the aqueous solution of zinc precursor and urea at 100 °C for 6 h, followed by annealing at 500 °C.[128]

2.2.4. 2D-templated synthesis:

In the 2D-templated technique, pre-synthesized nanomaterials or bulk materials were used as a template to grow anisotropic nanocrystals.[129, 130] Tom and co-workers prepared uniform large-area graphitic ZnO (gZnO) using graphene oxide (GO) as a template.[84] ZnO (<1 nm thickness) adopts a graphitic layered phase (gZnO). Interestingly, the gZnO is stable under ambient conditions and more ionic than other 2D nanomaterials (e.g., graphene, h-BN, silicene, or germanene), which led a drastic difference in physical and chemical properties as compared

to other atomic layer nanomaterials. The surface morphology of monolayer gZnO was characterized using SEM and AFM. The synthesized gZnO was 2.8 Å thick with ~20 μm lateral size (Figure 6 g-h). Nanobeam electron diffraction (NBED) pattern (Figure 6 i) displayed single crystal GO corresponding to [0002] plane and polycrystalline ZnO corresponding to {10 $\bar{1}$ 0} plane with d spacing 2.85 ± 0.08 Å. The STEM image and corresponding intensity profile indicate the layered structure of the ZnO crystal grown between the layers of rGO (Figure 6 j). gZnO has considerable potential to use at high temperatures in ambient or oxidative conditions due to its chemical stability and oxidation resistance. The behavior of ZnO sheets of different thicknesses was further studied at high temperatures (800 °C). The morphological changes before and after annealing treatment are analyzed by SEM (Figure 6 k-l). The streaks originated after annealing because of the charging effect, which was enhanced due to the coarsening effect (termed as rupture of the continuous film and increasing the thickness of poor conductivity to ZnO). The roughness value measured from the AFM gradually increases in the ZnO sample with a thickness higher than 1 nm. However, in the case of gZnO (thickness: 0.54 nm), the roughness of the sample is deduced with annealing, attributing to the low surface energy difference between gZnO and its bulk counterpart. The {0001} surface has low surface energy because of its layered structure, and it is challenging to endure coarsening or ripening to lower the surface energy. Thus, gZnO is a viable option for high-temperature ambient environment applications.

Liu and co-workers demonstrate an ultrathin porous ZnO nanosheet using GO as the template.[85] In synthesis, an aqueous solution of zinc precursor, HMTA, and GO was hydrothermally treated at 150 °C for 8 h. The sample exhibited well-dispersed two-dimensional nanosheet morphology with no aggregation (Figure 6 m). TEM study suggested the porous nature of the nanosheet (Figure 6 n-o). d-spacing of 2.76 and 2.59 Å corresponds to the (100)

and (002) plane of hexagonal ZnO, respectively (Figure 6 o). The height profile study suggests that the synthesized porous ZnO nanosheets are ~ 2.9 -3.4 nm thick.

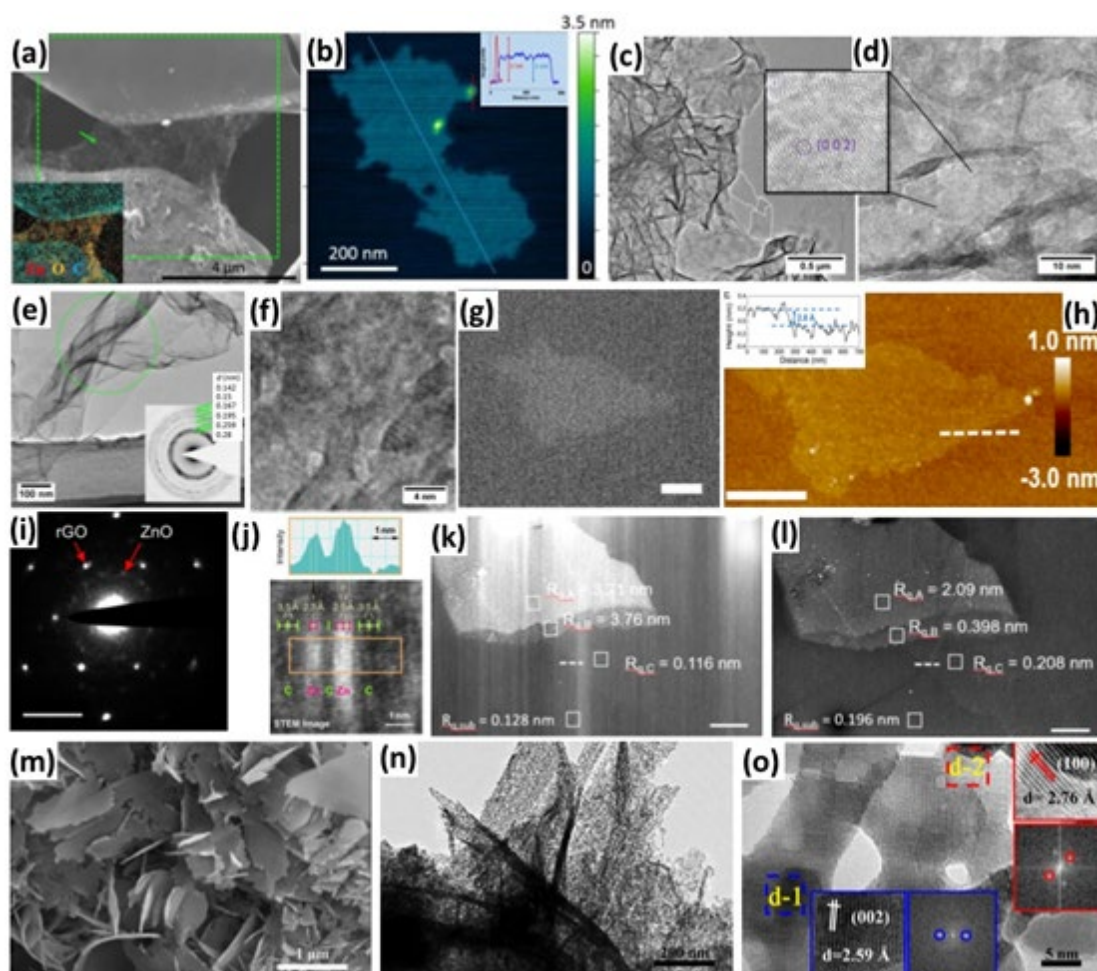


Figure 6. (a) SEM image with EDS elemental mapping (inset) (b) AFM image, inset: height profile image of ZnO nanosheet. (c) Low magnification TEM (d, f) HRTEM image of monolayer ZnO nanosheet with crystal lattice (inset). (e) TEM image with corresponding SAED pattern (inset), Reprinted from permission [83]. Copyright 2015, American Chemical Society.” (g) SEM image, (h) AFM image with corresponding line profile (inset image) of a monolayer of gZnO nanosheet (scale bar 1 μm), (i) Nanobeam electron diffraction pattern of 3-layer gZnO (scale bar 5nm^{-1}), (j) HRSTEM image of a ZnO and rGO composite with intensity profile diagram. SEM image of (k) as-synthesized (l) annealed at 800 $^{\circ}\text{C}$ of ZnO nanosheet

respectively. “Reprinted from permission [84]. Copyright 2019, American Chemical Society.”

(m) SEM, (n-o) TEM image of synthesized porous ZnO nanosheet on GO template. “Reprinted from permission [85]. Copyright 2019, American Chemical Society.”

In another study, Liu and co-workers reported a two-step method (hydrothermal and assembly) for synthesizing 2D single-crystalline ZnO nanosheets.[131] In their experiments, $\text{Zn}(\text{Ac})_2 \cdot 2\text{H}_2\text{O}$ and ethylene glycol (EG) was hydrothermally heated at 160 °C for 1 h to obtain EG-capped ZnO nanoparticles. Further, monodispersed polymer colloids, poly(styrene-methyl methacrylate-sulfo propyl methacrylate potassium) (P(St-MMA-SPMAP)) were added and stirred for 48 h. The solution was filtered and dried at 40 °C to get a layer of assembled ZnO/colloidal composites. During the filtration and drying process, layered ZnO/colloidal composites were formed due to the self-assembly of nanoparticles. Eventually, the resulting layered structures were annealed at 300 °C and 450 °C (Figure 7 a). TEM characterization show uniform, flat ZnO nanosheet (with 20-50 nm pore sizes) grown along $[10\bar{1}0]$ (Figure 7 b) and $[\bar{1}2\bar{1}0]$ (Figure 7 c) plane. $\{\bar{1}2\bar{1}0\}$ and $\{10\bar{1}0\}$ facets of nanosheets were nonpolar surfaces that exhibit lower surface energies than the polar surface of the positive charged Zn-(0001) surface and negatively charged O-(000 $\bar{1}$) surface. However, the nucleation of EG-capped ZnO nanoparticles and the calcination of colloidal spheres results in the formation of mesopores and the exposure of $\{0001\}$ polar facets within mesopores. Thus, colloidal spheres are responsible for forming mesopores and exposed $\{0001\}$ polar facets. HRTEM image (Figure 7 d-h) displays a perfect ZnO crystal lattice along with some contrast changes, and these changes are due to thickness, distortion of crystals, and dislocations.

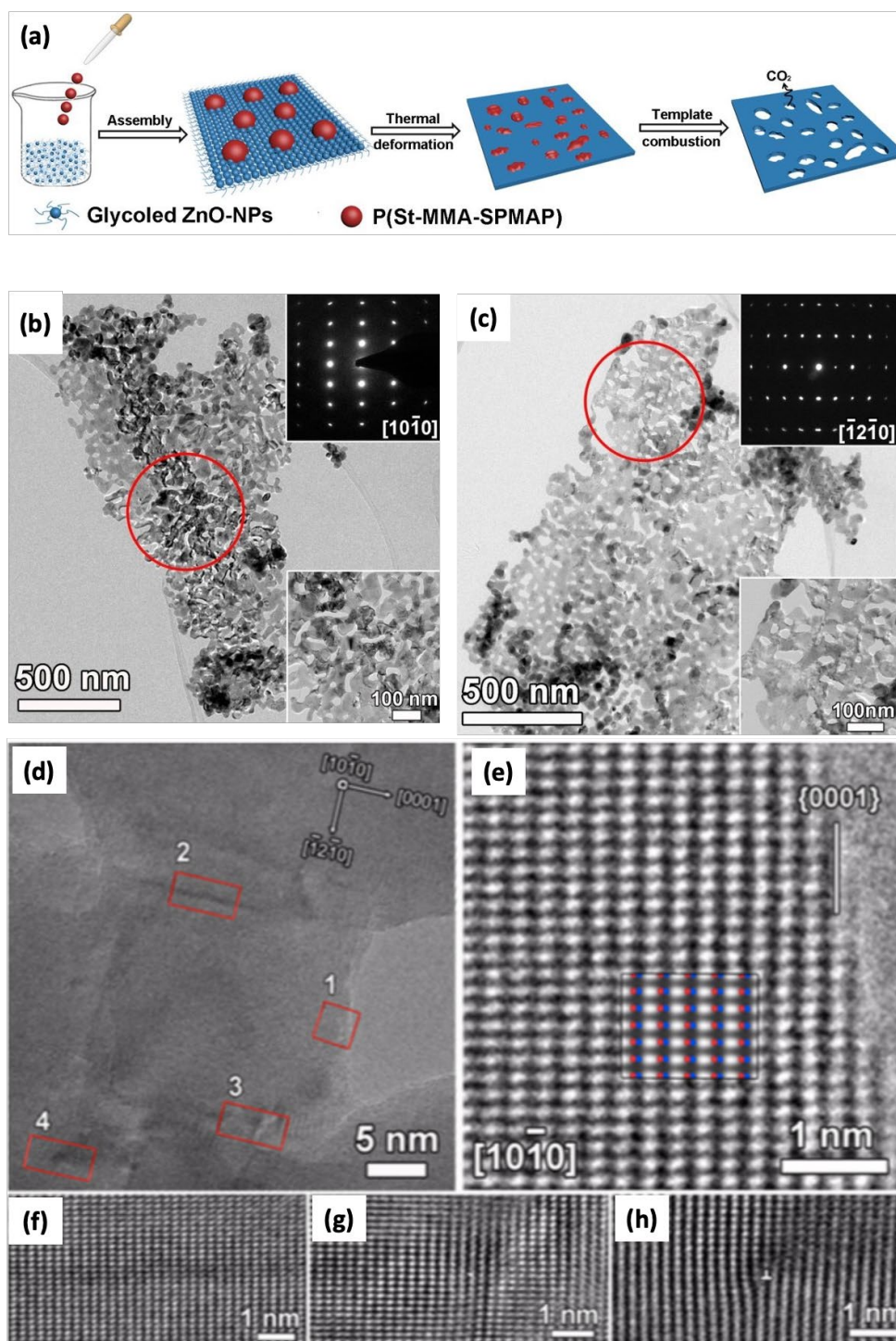


Figure 7. (a) Schematic representation of ZnO-MSN synthesis, (b,c) low magnification and (lower inset) enlarged image of the selected area, (upper inset) SAED pattern. (d) HRTEM image of ZnO-MSN, (e) atomic resolution TEM image and (f-h) magnified atomic-resolution TEM images. “Reprinted from permission [131]. Copyright 2016, Elsevier.”

2.2.5. Chemical Bath Deposition (CBD):

Chemical bath deposition (CBD) is one of the solution phase methods used to prepare compounds from aqueous solutions. Huang and co-workers synthesized a ZnO nanosheet on the copper substrate through chemical bath deposition.[75] In this synthesis, an aqueous solution of Zn precursor and urea is used as a reaction solution. The freshly cleaned copper foil was immersed into the reaction solution with continuous stirring at 80 °C. After deposition, the film was washed with distilled water and annealed at 350 °C for 45 min in Ar atmosphere. Urea is typically used as a precipitation agent for uniform film growth. During the annealing process, water and carbon dioxide were released from the deposited film, and a pure porous zinc oxide nanosheet was formed on the copper substrate. The SEM and TEM studies suggest that the porous ZnO covered the surface of Cu foil. SAED pattern confirms the polycrystalline nature with the wurtzite structure of porous ZnO nanosheet.

2.3 Other synthesis Methods:

Wang and co-workers prepared a free-standing single-layer ZnO sheet via oxidation of hydrothermally grown few-layer zinc chalcogenides.[87] In a three-step process that involves (i) hydrothermal synthesis of ZnS n-propylamine (pa) intermediate, (ii) ultrasonic exfoliation to obtain lamellar hybrid ZnS (pa), (iii) thermal treatment (600-950 °C) of lamellar ZnS (pa) to obtain ZnO (pa). TEM image showed a large area, free-standing folded ZnO sheet (Figure 8 a). HRTEM analysis indicated that the 0.282 nm d spacing corresponded to the (100) plane of wurtzite ZnO, which revealed that the surface of the ZnO layer was perpendicular to the c axis. AFM topological analysis confirmed the occurrence of several micrometers lateral size with ~2 nm thickness of the ZnO nanosheets (Figure 8 b). Here, n-propylamine acts as a spacer to prevent the interactions between neighboring inorganic fragments and help stabilize the layered ZnO structure. The sample was calcinated in the 600-950 °C temperature range to understand

the temperature effect. The sample calcinated at a higher temperature has a reduction in cell volume. However, the morphology of the ZnO sheet remains the same due to the ultrathin thickness and free-standing nature. If the film thickness is less than the critical thickness, structural strain is endured by the ZnO sheet, which is released by generating defects that can be fixed by calcining the sheets and the freestanding nature of the nanosheet. The effect of different reaction temperatures on ZnO layers was studied. A thick, layered ZnO structure was observed when the reaction temperature was below 110 °C. As the reaction temperature increased above 110 °C, a single-layered structure was observed. Moreover, only nanoparticles were found when the reaction temperature reached 140 °C.

Zhou and co-workers prepared large-area metal oxide nanosheets using glucose, urea, and metal salts.[88] In a typical synthesis, zinc precursor, glucose, and urea were pre-annealed at 140 °C for 6 h to get a porous framework. The synthesized porous material was further annealed at 500 °C for 10 h (Figure 8 c). Notably, glucose played a crucial role for the following reasons: (i) due to the low melting point, glucose undergoes thermal polymerization to give molten syrup. (ii) Glucose molten syrup form bubbles in the presence of gases evolving from the evaporation and decomposition of urea and forming ultra-thin membrane, and finally, porous carbon foam with metal salt was formed (iii) Oxygen functional group present in the molten glucose syrup is favorable for the homogeneous distribution of metal salt. Importantly, no carbon foam was observed without adding the urea, confirming urea's crucial role in forming carbon foam. Folded 2D ZnO nanosheet was observed in SEM analysis (Figure 8 d). Next, the TEM image of ZnO nanosheets suggests that the nanosheets were composed of small nanoparticles with a mean size of 9.6 nm (Figure 8 e). The polycrystalline nature of the material was confirmed by the corresponding diffraction pattern (Figure 8 f). HRTEM image confirms the d-spacing of 0.281 nm corresponding to the (100) plane of ZnO (Figure 8 g-h). The

temperature effect on the samples was studied for pre- and post-annealing. It is observed that the carbon foam was not formed if the temperature was below the pre-annealed temperature. However, increasing the temperature to 600 °C has resulted in a porous structured nanosheet.

Zhu and co-workers synthesized ZnO nanosheets by cathodic electrodeposition using a triphasic electrode system with an air-liquid-solid (A-L-S) interface.[89] In the typical electrochemical synthesis, superhydrophobic carbon fiber as a working electrode, platinum wire as a counter electrode, and saturated calomel electrode as a reference electrode and aq. $\text{ZnCl}_2\text{-KCl}$ as an electrolyte was used. The deposited substrate was heated at 400 °C to remove HCl and H_2O . The hexagonal $\text{Zn}_5(\text{OH})_8\text{Cl}_2$ nanosheet arrays' synthesis mechanism was studied at different current densities ranging from -0.3 to -10 mA/cm^2 . At low current density (-0.3 mA/cm^2), a low concentration of OH^- was produced, which resulted in the formation of a small number of hexagonal $\text{Zn}_5(\text{OH})_8\text{Cl}_2$ nanosheets. It is noticed that the regular hexagonal $\text{Zn}_5(\text{OH})_8\text{Cl}_2$ nanosheets were formed at higher current densities, i.e., -0.5 to -7 mA/cm^2 , likely due to higher interfacial pH values. Further, at a current density of -10 mA/cm^2 , ZnO nanoparticles with a diameter of about 70 nm were obtained. Interestingly, the hexagonal $\text{Zn}_5(\text{OH})_8\text{Cl}_2$ nanosheets obtained at a current density of -2 mA/cm^2 can be transformed into mesoporous ZnO nanosheets by thermal treatment (400 °C). HRTEM image reveals $d = 0.28$ nm, corresponding to the (101) plane of wurtzite ZnO.

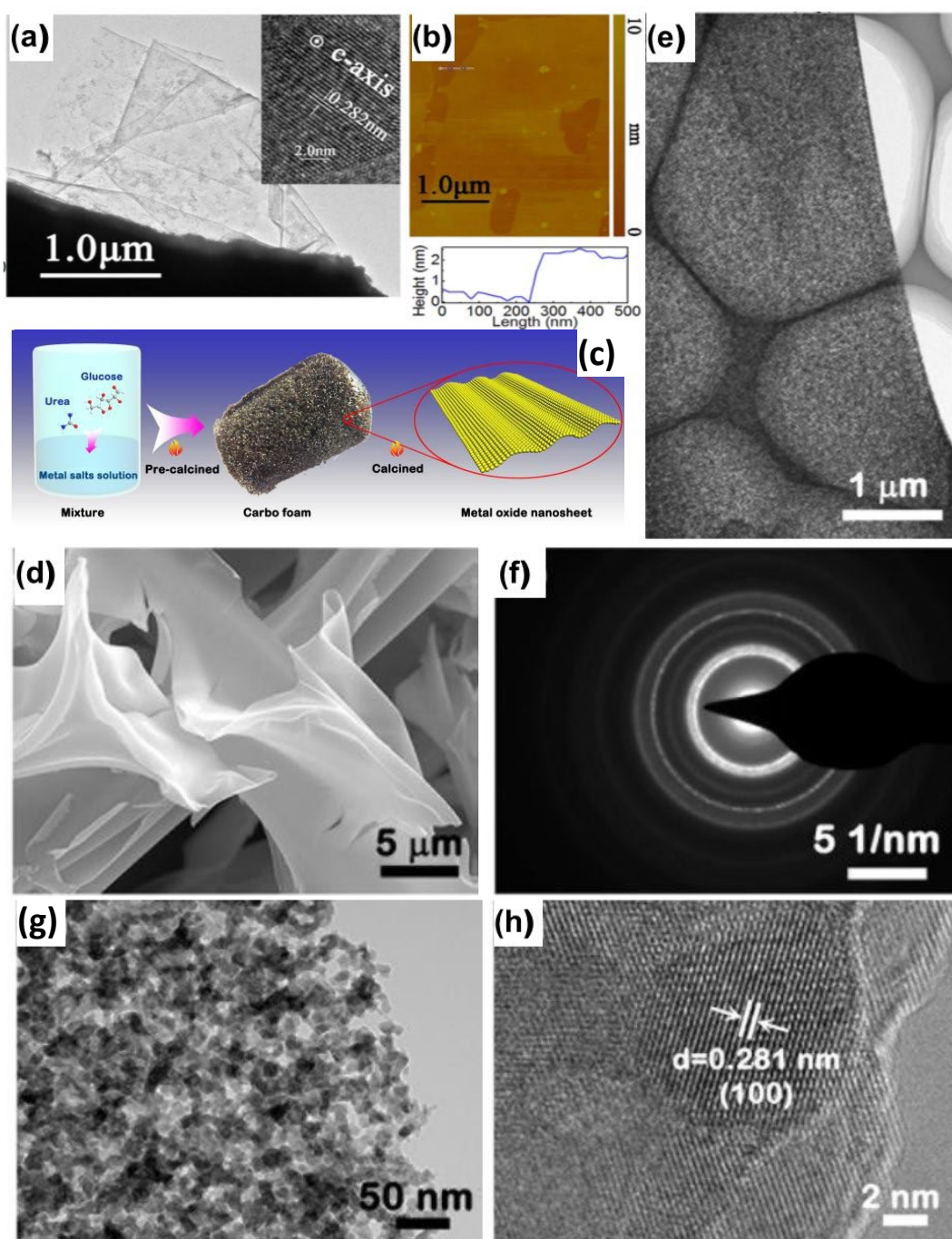


Figure 8. TEM image of (a) ZnO (scale bar 1 μm) with SAED pattern (inset image), (b) AFM image of ZnO thin layers. “Reprinted from permission [87]. Copyright 2017, American Chemical Society.” (c) Schematic representation of formation mechanism of transition metal oxide, (d) SEM, (e) TEM, (f) SAED pattern, (g) Enlarged TEM, (h) HRTEM image of ZnO nanosheet. “Reprinted from permission [88]. Copyright 2016, Royal Society of Chemistry.”

2.4. Physical techniques:

2.4.1. Chemical Vapour Deposition (CVD):

Chemical Vapour Deposition (CVD) is a technique in which thermally induced reactions are employed to synthesize high-quality, defect-free large-area and single-layer 2D nanomaterial.[48, 51, 52, 132] Park and co-workers had reported use of ZnO, graphite powders and gold coated Si substrate in an alumina boat at 800-950 °C under optimized O₂ and Ar mixture flow to obtain nanowires and nanosheets. The lateral size of nanosheet was found to be 50–100 μm with 50–100 nm in thickness. The growth mechanism of ultrawide nanosheets can be illustrated with three progressive mechanisms as follows: (i) formation of basal nanowire using vapour-liquid-solid process along with catalyst, (ii) side branching via vapour-solid process using supersaturation, and (iii) planar filling by selective condensation process.

Here, supersaturated reactant vapors perform a crucial role in development of dendritic side branches. From this perspective, gold catalyst is not essential in the development of ZnO growth process and branch growth. It should be based on a surface diffusion as a function of growth period and annealing temperatures.[44] Wang and co-workers reported the synthesis of ZnO nanosheet by the typical chemical vapor deposition (CVD) method.[86] In the synthesis, the precursor mixture of ZnO powder, graphite, and phosphor pentoxide (P₂O₅) with the desired ratio was heated at 1000 °C for 30 min in an argon (Ar) and oxygen (O₂) atmosphere. P₂O₅ plays a crucial role in the formation of ZnO nanosheets. Pure ZnO powder shows trigon-star-like morphology along with ~5 μm branch lengths (Figure 9 a). However, upon P doping, a smooth surface, thin, large area ZnO nanosheet was formed with ~50 nm thickness (Figure 9 b). In ZnO/GO nanocomposite, the ZnO nanosheet was entirely covered by a flexible GO sheet which reduces the brittleness of ZnO. As a result, the mechanical property of the nanosheet

was improved (Figure 9 c). A ZnO/GO nanocomposite decreases the surface energy, consequently improving the stability.

2.4.2. Atomic Layer Deposition (ALD):

Atomic layer deposition (ALD) is widely used for the deposition of thin films from the vapor phase, in which deposition is subjected to a gas-surface reaction. ALD mainly offers a controllable thickness during thin film deposition.[133] Naeem and co-workers synthesized ZnO nanomembranes (NMs) of different thicknesses using the atomic layer deposition method (ALD) with different ALD cycles on a polyurethane sponge matrix.[134] In a typical synthesis experiment, an aqueous solution of diethylzinc was added into the deposition chamber at 150 °C with the help of N₂ carrier gas with a flow rate of 20 sccm. After ALD deposition, the polyurethane sponge matrix was removed and calcined under an O₂ atmosphere (600 mL/min) at 700 °C for 3 h. Morphology characterization suggested that the ZnO nanomembranes had lateral size in tens of microns and thicknesses of 8.7, 17.4, and 34.8 nm after 50, 100, and 200 ALD cycles.

2.4.3. Pulsed Laser Deposition (PLD):

Pulsed laser deposition is another effective technique for depositing large-scale thin film under a higher vacuum and lower growth temperature. In this technique, a small amount of precursor is used for deposition due to attaining the rapid heating stoichiometry growth.[135] Weig and co-workers prepared flat, triangular ZnO nanosheets under high pressure via the catalyst-assisted pulsed laser deposition method.[136] The experiments heated 2.5 nm thick gold (Au) coated sapphire substrate at the desired temperature. Further, ZnO deposition was carried out by laser ablation at an absolute pressure of 0.5 bar of (i) pure oxygen and (ii) 5 % O₂ - 95 % Ar ambient for 15 min to 1 h. The entire surface was covered in a pure O₂ atmosphere

by a densely packed array of ZnO nanosheets with $4.5 \pm 1 \mu\text{m}$ average lengths (Figure 9 d). ZnO nanosheet showed flat and triangular morphology with an average thickness of $51 \pm 10 \text{ nm}$ and $30 \pm 9 \text{ nm}$, with a width of $508 \pm 130 \text{ nm}$ and $34 \pm 6 \text{ nm}$ at the base and tip, respectively. TEM characterization demonstrated single-crystalline nature and stacking-free nanosheets with bending contours (Figure 9 e-f). Figure 9 e shows the inclination angle α of the growth direction with the ZnO hexagonal c-axis. Growth of the nanosheet was along [0001] direction (Figure 9 j). The Au-ZnO interface of the nanosheets produced at high oxygen partial pressure is observed to be a single ZnO (1011) facet. Au particles present at the tip of every sheet (Figure 9 j) confirm the catalyst-assisted growth mechanism. Thin Au layer self-organizes and forms small droplets while heating the substrate leading to the nucleation at the catalyst interface and nanostructure growth beneath the catalyst droplet where the axial growth rate is the highest and direction inclined to the ZnO hexagonal c-axis, which allows two opposites. Different facets of the sidewalls grow differently with smooth surfaces, which are obtained due to the high substrate temperature and supersaturation. ZnO {0001} plane would amplify the growth of two sidewalls without the addition of other facets resulting in anisotropic radical growth of the ZnO nanosheet also if sidewalls formed at the initial stage of the growth process i.e., near the substrate, large width at base, flat, triangular nanosheet were formed.

A few ZnO nanowires were also noticed due to the partial pressure of the reduced oxygen on the growth chamber. The average diameter of the nanowire was $55 \pm 15 \text{ nm}$ and $28 \pm 7 \text{ nm}$ at the base and tip, respectively, along with $2.1 \pm 0.7 \mu\text{m}$ length. HRTEM image and SAED pattern confirmed the single-crystalline nature of the nanowire grown without stacking faults, as shown in (Figure 9 g-h). TEM has been used to investigate the Au-ZnO interface of a nanowire growing in the ZnO [0001] direction (Figure 9 i). The interface consists of a single ZnO (0001) facet surrounded by the Au droplet. As mentioned, the formation of the most stable growth facet at the catalyst nanowire interface is consistent with this observation. The

formation mechanism of the nanowire was similar to the nanosheet and followed catalyst-assisted growth. The growth rate could be tuned by surface energy and stability of the sidewalls. Hence, all side facets of the nanowire are made up of similar ZnO crystal planes having the same surface energies and VS growth rates. Radial growth of the nanostructure was identical (i.e., $VS_B = VS_A$), and axial and radial growth rate ratios governed the tapering of the nanowire. From the above possible mechanism, it can be concluded that the morphology of ZnO nanostructure single-crystalline ZnO nanosheets was formed due to high oxygen partial pressure, whereas [0001] directional ZnO nanowires were formed at low oxygen partial pressure as shown in (Figure 9 i-j).

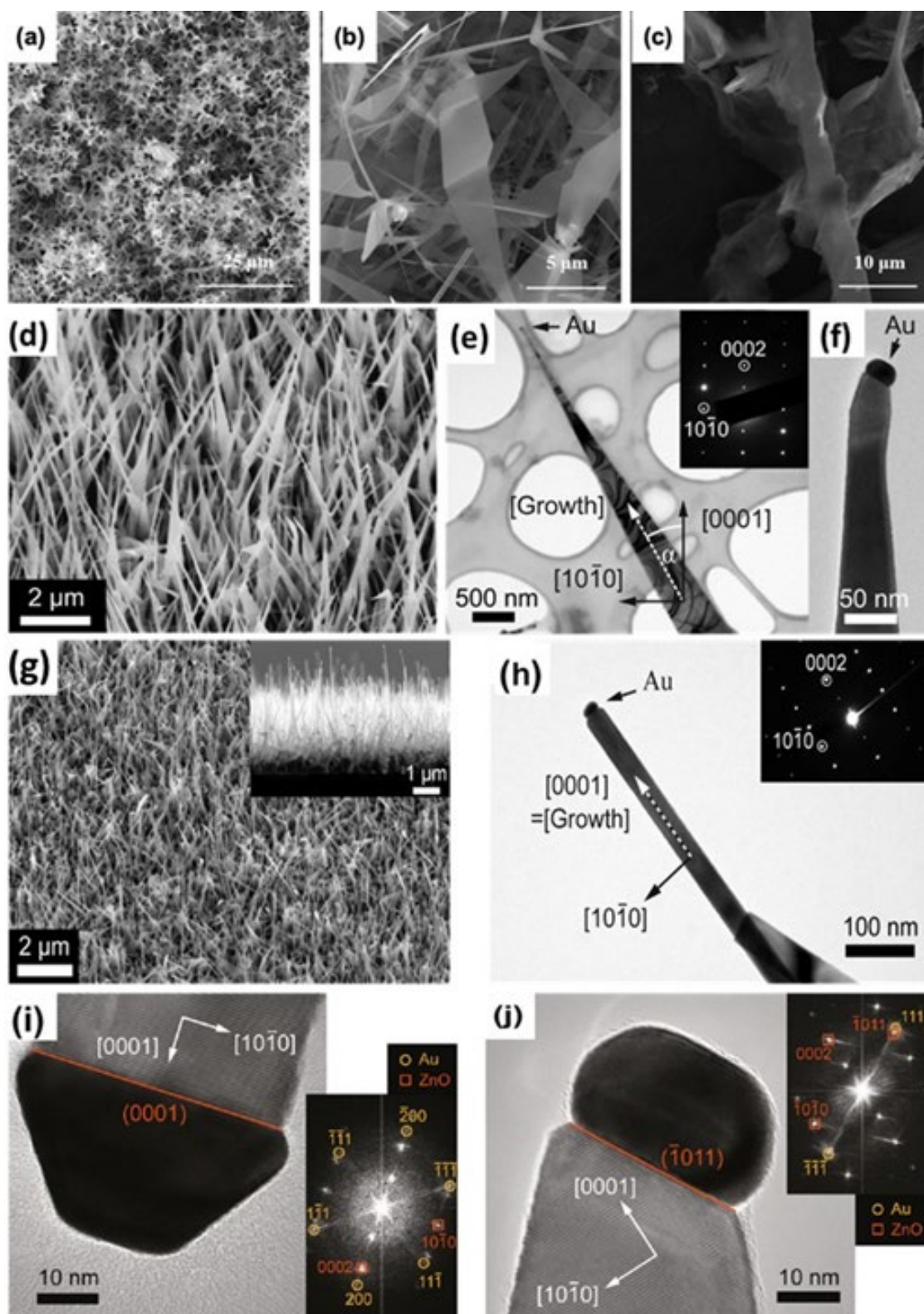


Figure 9. SEM image of (a) pure ZnO, (b) ZnO nanosheet, (c) Low magnification ZnO/GO nanocomposite. “Reprinted from permission [86]. Copyright 2016, Elsevier.” (d) SEM imaging of ZnO grown at 800 °C in a 0.5 mbar pure O₂ environment with a 45° slanted view, (e) Bright-

field TEM picture of a single ZnO nanosheet with corresponding SAED pattern, revealing the inclination angle of the growth path with the ZnO hexagonal c-axis, (f) A bright-field image of a nanosheet tip reveals a kink beneath the Au catalyst droplet, (g) SEM images of a sample grown at 800 °C in a 0.5 mbar mixed ambient of 5 % O₂ - 95 % Ar, with a 45° tilted view and cross-sectional (inset) image, (h) A bright-field TEM image of a single nanowire with its accompanying SAED pattern, (i) HRTEM micrograph of a nanowire and its Fourier transform, grown in a 0.5 mbar mixed ambient of 5 % O₂ - 95 % Ar, (j) HRTEM image and its Fourier transform of a nanosheet grown in a 0.5 mbar pure O₂. “Reprinted from permission [136]. Copyright 2011, American Chemical Society.”

In the above section, we highlight different bottom-up synthesis methods for preparations of 2d nanosheets. Here, in the self-assembly section, we highlight the ease of tuning the morphology and functionality of the molecules depending upon their self-assembly characteristics and show their novel properties which will shed new light on material design and potential applications. Distinct from the self-assembly method, the 2D-oriented attachment method will open alternative ways to rationally design in 2D nanosheets of single or multicomponent materials with their novel structures, controlled lateral size, and multifunctionalities benefiting different applications. The solvothermal method's temperature, reaction time, and precursor concentration can tune the size, shape, and crystallinity. Further, physical techniques (CVD, ALD, PLD) are mainly employed to synthesize high-quality, defect-free, large-area thin films, which offer large surfaces for designing devices with complex components without any detrimental consequences on performance.

3. Applications

Due to the unique physical, chemical, optical and electronic properties of ultrathin 2D ZnO nanosheets are noted to be promising nanomaterials for various practical applications.[1, 137] This section reviews the promising applications of 2D ZnO nanostructures in various fields, such as electronics/optoelectronics, catalysis, energy storage, conversion, etc.

3.1 Energy storage:

The development of large-scale and cost-effective energy storage devices is an exotic topic worldwide due to the increasing energy demand.[138-142] To this end, Lithium-ion batteries (LIBs) are recognized as the most essential and attractive energy storage devices due to their long lifetime and higher energy density as compared to other rechargeable batteries.[143-148] Most marketable LIBs are based on conventional graphite anode material and display a theoretical capacity of 372 mA h/g.[149] Moreover, ultrathin 2D ZnO nanostructures-based anode materials have received much attention in recent years because of their high exposed surface area, which facilitates faster ion transport, shortens the charge transport path length, and has a low cost.[150] Further, interlayer spacings of 2D nanomaterials provide superior ion transport channels for ion-intercalation energy storage devices. Structural flexibility, turnability, and stability make them promising candidates for flexible and lightweight devices.[151] As a typical example, Xia and co-workers reported the fabrication of ZnO nanosheets grown in situ on Ni foam and displayed ~1507 mA h/ g reversible capacity for the first cycle. Further, it shows a stable capacity value of 1292 mA h/g at a current density of 0.2 A/g (i.e., 85.7 %) even after 45 cycles (Figure 10 a-d), indicating excellent stable electroactive performance.[74] Further, the rate performance of the ZnO nanosheets@Ni foam was studied at different current densities. It exhibits specific capacitance ranging from 158 to 1375 mA h/g when the current density was reduced from 4.0 A/g to 0.2 A/g (Figure 10 e).

Further, Huang and co-workers performed a comparative study of the electronic properties of ZnO powder and ZnO nanosheet grown at copper substrate as an anode material in LIBs[75]. Figure 10 (f) and (g) showed the charge and discharge capacities of ZnO nanosheet@Cu and ZnO powder, respectively. Porous ZnO nanosheets showed higher charge-discharge capacities as compared to ZnO powder. Porous ZnO nanosheet exhibited 400 mAh/g capacity retention up to 100 cycles. On the other hand, ZnO powder exhibited 170 mAh/g capacity retention after 50 cycles (Figure 10 h). Rate capability was studied at different current densities (0.05 to 2 A/g), as shown in Figure 10 i. The electrochemical performance of ZnO nanosheets was enhanced because of their porous nature. Due to the net-like morphology, electric contact between active materials was more as well as the electrolytes could quickly be passed through the pores and form large contact interfaces between the electrode and electrolyte, which shortens the diffusion paths of lithium ions. Consequently, electrochemical reactions of active materials were carried rapidly, which gives higher capacity and enhanced rate capability. In addition, porous nanosheets have good endurance of volume change which is attributed to good cyclability.

In addition to LIBs, the application of ZnO nanomaterials can also be seen in Zn ion battery as well. For example, Xie et al coated 3D nanoporous ZnO on top of Zn anode to suppress the side reactions on the interface (associated with interaction of Zn metal and water).[152] The unique structure also improves the kinetics of Zn deposition due to this ~100 % utilization efficiency was achieved. Kim et al prepared Zn hexagonal pyramid array (HPA) coated with a functionalized ZnO layer which suppresses the dendritic growth in Zn//Zn symmetric cell.[153] To the best of our knowledge, 2D ZnO nanosheets were not utilized in Zn ion battery yet. We believe that application of 2D ZnO nanosheets could be advantageous as micro-sized ZnO layer

can be too thick that it passivates the Zn metal surface and increases the nucleation overpotential for Zn deposition.

Supercapacitors are other promising energy storage devices due to their high power density, fast charging time, and long lifetime.[154] As per the Ragone plot, the supercapacitor has a higher power density than typical capacitors and batteries, which is very beneficial in transportation, backup power stations, and elevators.[154] Due to their ultrathin-specific surface area, 2D metal oxide/hydroxide plays a crucial role in high-performance supercapacitors.[155] Naeem and co-workers investigated the electrochemical performance of ZnO nanomembrane (NM) at different thicknesses tuned by changing deposition cycles (i.e., 50, 100, 200 cycles).[134] It delivered 104, 846, and 195 F/g specific capacitance with 1 A/g current density at 50, 100, and 200 cycles, respectively. Zn nanomembranes at 100 cycles give high specific capacitance due to their flexibility with the increased surface area, which aids in easy electron transportation during the charging/discharging process and lowers interfacial resistance (Figure 10 j-k). In addition, at the 100th deposition cycle, energy density decreased from 42 to 5 Wh/kg while the power density increased from 300 to 1500 W/kg, as the current density increased from 1-5 A/g (Figure 10 l). Further, the authors explored the effect of different electrolytes, such as KOH, KCl, and Na₂SO₄, on the performances of ZnO NMs electrodes. The ZnO nanomembrane electrode in the KOH electrolyte gave the highest capacitance (846 F/g) as compared to KCl (456 F/g) and Na₂SO₄ (65 F/g), suggesting that the KOH is a suitable ion exchanger among others.

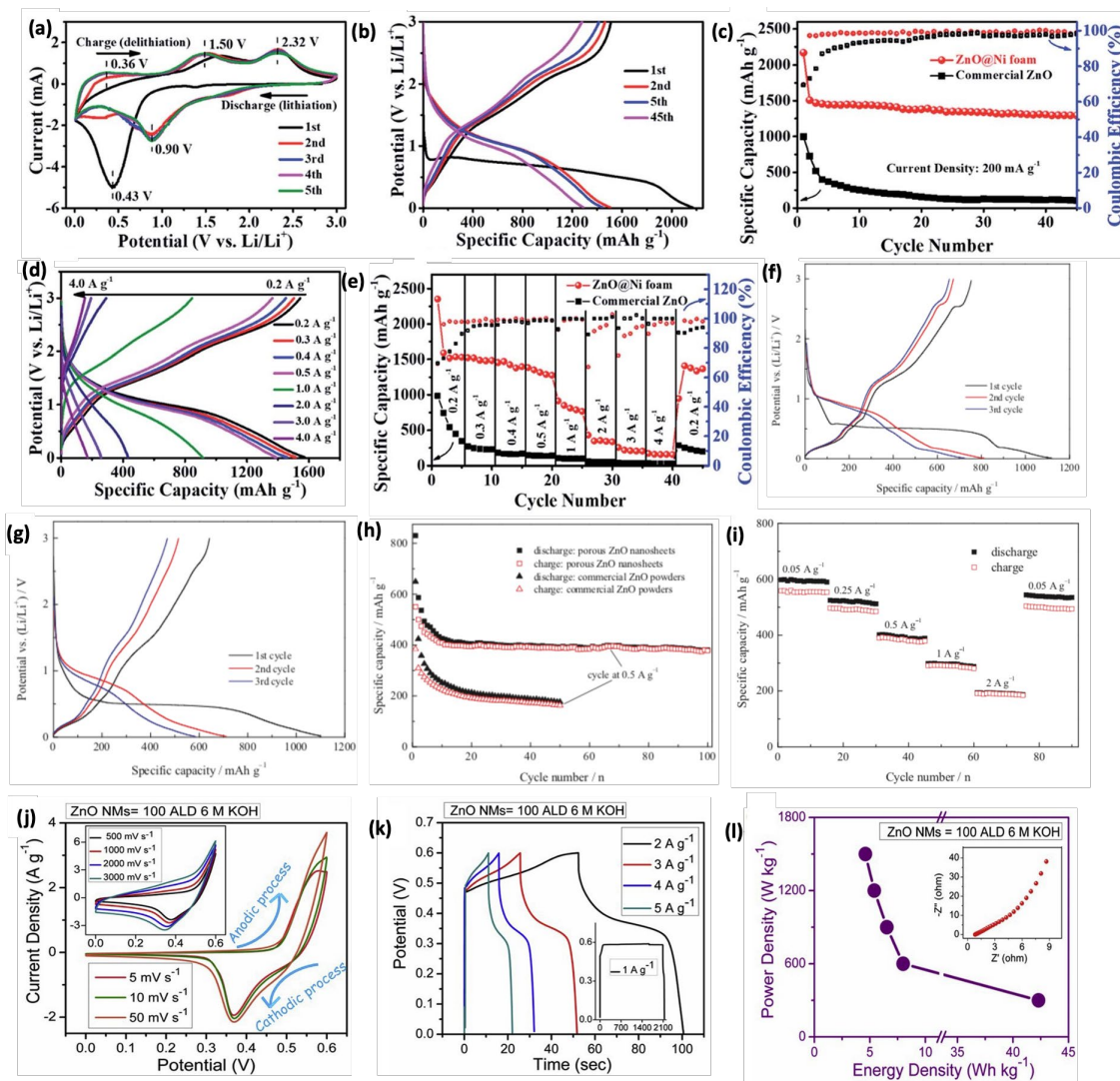


Figure 10. Electrochemical performance of ZnO (a-e) nanosheet, (a) Cyclic Voltammetry at 0.1 mV/s, Galvanostatic charge-discharge curve at (b) 0.2 A/g for different cycles, and (d) different current densities, (c) Cyclic stability at 0.2 A/g, (e) Rate performance at different current densities. “Reprinted from permission [74]. Copyright 2019, Royal Society of Chemistry.” Galvanostatic charge-discharge curve at 0.05 A/g, (f) porous ZnO nanosheets and (g) commercial ZnO powders, (h) Cyclic stability of porous ZnO nanosheets and commercial ZnO powders at the current density of 0.5 A/g, (i) Rate performance of ZnO nanosheet. “Reprinted from permission [75]. Copyright 2011, Elsevier.” (j) CV, and (k) GCD curve of

ZnO nanomembrane, (l) Regone plot of Energy density vs. power density "Reprinted from permission [134]. Copyright 2020, Elsevier."

3.2 Electronic/Optoelectronic Devices:

Optoelectronics devices are a transducer that converts optical signals to electric signal and vice versa. Optoelectronics devices consist of LEDs, field-effect transistors (FETs), and photodiodes. The performance of optoelectronic devices is mainly dependent on the material's light absorptivity and photoelectric conversion capability.[156] 2D ZnO nanosheets are widely being used in optoelectronic devices as well as photodetectors due to their wide direct bandgap (3.37 eV), large exciton bandgap energy(60 meV), high breakdown voltage, multifunctionality, thickness-dependent tunable bandgap from indirect to direct along with flexibility and optical transparency which facilitates device fabrication. [69, 157] After heating at 95 °C for 48 hours, FETs based on large area ZHDS manufactured on a plastic substrate by the ILE approach (Figure 11 a) have demonstrated an enhanced on/off ratio from 103 to 3105 with increased mobility value from 0.0027 to 0.12 cm²/V.s [108] In both the cases (Figure 11 c-d), the drain current was same which suppressed the low gate bias region of the annealed device, consequently, power was saved at an off state. Further, the same group had reported that the ultrathin ZnO nanosheet on Si wafer coated with the thickness of 50 nm Al₂O₃ by ILE method exhibited the 4.5 ×10¹² cm⁻² carrier concentration and 0.10 cm²/V.s hole mobility of the nanosheets (Figure 11 e-g).[68] This low mobility arises due to the presence of surfactant at the surface of the ZnO nanosheet, leading to poor electrical contact between the nanosheet and electrodes. Similarly, Tian and co-workers synthesized a highly crystalline ZnO nanosheet. The resulting ZnO nanosheet shows high mobility of 588.9 cm² V/s with an on/off ratio >10⁷, which makes them a promising candidate for application in data storage with non-volatile

features.[69] Herein this work authors reported high ionic mobility in comparison to nanowires and nanobelt morphology which can be attributed to the low density traps, defects and highly crystalline nature of ZnO nanosheets. Additionally, Pillai and co-workers fabricated ZnO thin-film-based transistors using tantalum oxide as a gate insulator.[158] It demonstrated low mobility of $\sim 1 \times 10^{-11} \text{ cm}^2/\text{V.s}$ with an on/off ratio of 10^8 - 10^9 . Further, Sun and co-workers analyzed the efficiency of transparent, flexible ultraviolet (UV) photodetectors prepared by depositing the atomically thin 2D ZnO nanosheets on a monolayer of graphene back electrode.[79] The photocurrent responses of the ultraviolet photodetectors oscillating between on and off ultraviolet light with an interval of 10 s and a bias of 0.5 V (Figure 11 h). No degradation was found during the on-off switching cycles (Figure 11 i), which confirmed the devices' tremendous stability and fast response speed. Furthermore, Khokhra and co-workers reported the comparative performance of different photodetectors prepared by undoped ZnO nanostructures such as nanosheets, nanoflowers, and nanoparticles under UV, white and green illuminations with voltage bias 5 V.[159] It was found that defect states oxygen vacancies (V_{O} s) and zinc interstitials (Zn_i s) plays a crucial role in the photodetector. The increase in the defect states increases the photo-response; however, excess defects diminished the photodetector performance. ZnO nanosheet-based photodetector exhibit moderated amount of defect states V_{O} s ($\sim 47\%$) and Zn_i s ($\sim 13\%$) than ZnO nanoparticles and nanoflowers, leading to faster response to photovoltage growth time and decay time under the UV and visible-light illumination (Figure 11 j-l). The authors did not study the reason for ZnO nanosheets higher performance to nanoparticles and nanoflowers.

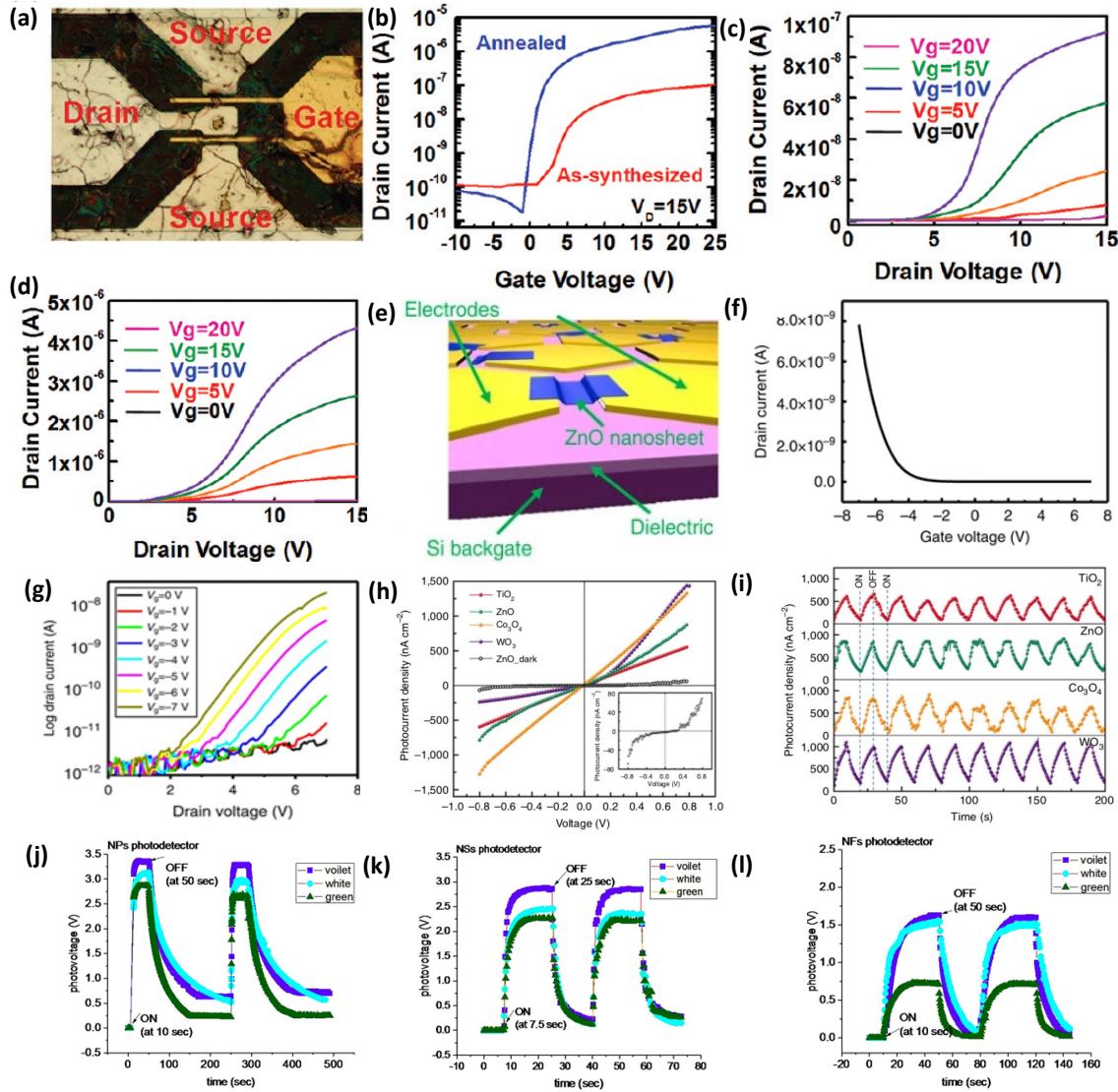


Figure 11. (a) Optical microscope image of ZHDS NM-fabricated FETs on a PET substrate. Transfer characteristics of (b) As synthesized and annealed at 95 °C for 48 h ZHDS. (c) ZnO nanosheet. Output characteristics of (c) as-synthesized (d) annealed ZHDS sample at different $V_D = 0-15 V$ and $V_G = 0-20 V$ “Reprinted from permission [108]. Copyright 2012, Chemical Society.” (e) Optical microscope image of ZnO nanosheet on Si wafer coated with 50 nm Al_2O_3 (f) plot of I_D Vs V_G at $V_D=5 V$ and $V_G = 7$ to $-7V$. (g) Plot of I_D Vs V_D at $V_G= 2$ to $-7 V$ with a 1 V step. “Reprinted from permission [68]. Copyright 2016, with permission from Nature Research.” (h) I-V Characteristics of 2D nanosheets. Magnified ZnO nanosheet (inset). (i) The plot of photoresponse study of 2D nanosheets. “Reprinted from permission [79]. Copyright

2014, Nature Research.” (j-l) Comparison of the relation between photovoltage and time of ZnO photodetectors thin films for UV, white and green illuminations. (j) NPs photodetector (k) NSs photodetector and (l) NFs photodetector. “Reprinted from permission [159]. Copyright 2017, Nature Research.”

3.3 Photocatalysis:

Photocatalysis is one of the promising strategies for the degradation/remediation of environmental pollutants. The photocatalysis process follows a three-step process (i) Charge carriers generated during the photoexcitation, (ii) Separation of the charge carriers and shifting of the charges towards the surface of the ZnO photocatalyst, (iii) Ease oxidation and reduction reaction on the catalyst surface.[1, 160, 161] 2D ZnO nanosheets play a more efficient role in photocatalysis than their bulk counterparts because of their large surface area with atomically thin thickness and highly active surface site. Also, charge carriers shifting distance is reduced due to atomically thin thickness than the bulk counterpart, resulting in better charge separation. Due to its wide bandgap and high exciton binding energy, the 2D ZnO nanostructure absorbs UV rays from a wide range of the UV spectrum, which improves photocatalytic performance. Moreover, the high mobility of the 2D ZnO nanosheet accelerates the electron transfer, which helps to improve quantum efficiency.[162] For example, a mesoporous 2D ZnO nanosheet synthesized in A-L-S triphase system was used to degrade Rhodamine B (RhB) dye under ultraviolet (UV) light.[89] It was found that 95% degradation was done in 120 min, 2.8 times more than at nitrogen-liquid- solid (N-L-S). The correlation coefficients of the A-L-S reaction are seven times higher than the N-L-S reaction. As a result, A-L-S triphase photocatalytic reaction interface is favorable for photodegradation kinetics. In addition, 2D ZnO mesoporous nanosheet (ZnO-MSN) synthesized by the colloidal template method was used for the comparative study of selective adsorption and photocatalytic degradation of differently charged

organic molecules (cationic rhodamine B (RhB), anionic methyl orange (MO), and neutral phenol).[131] The study was carried out with individual as well as mixed pollutant molecules. In a single pollutant, the adsorption capacity of ZnO-MSN was higher for RhB (23.2 %) compared to phenol (16.9 %) and MO (7.1 %). On the other hand, in mixed pollutants, it was 18.8 % for RhB, 10.7 % for phenol, and 1.6 % for MO, which implies that the negatively charged O surface of ZnO-MSN formed coulombic attraction toward positively charged RhB. Further, a photodegradation study was performed using single and mixed pollutants. RhB showed a 5.8×10^{-2} degradation rate in individual pollutants, while MO and phenol showed 4.1×10^{-2} and 1.7×10^{-2} degradation rates, respectively. RhB, MO, and phenol show 2.0×10^{-2} , 0.94×10^{-2} and 0.68×10^{-2} degradation rates in the presence of mixed pollutants. Moreover, using the SILAR method, the ZnO nanosheet was grown on a different substrate (polyurethane foam and glass) and used for acid orange 7 (AO7) dye degradation under UV light. Interestingly, 93 % and 45 % degradation were shown by ZnO nanosheet grown on polyurethane foam and glass substrate after 135 min.[163] Further, in the recycled study, ZnO@foam showed 34 % and 31 % degradation in the second and third cycles, respectively, while ZnO@glass degraded 20 % in the second cycle. In addition, ultrasonically synthesized three different ZnO nanostructures by adjusting the solution pH: nanoplates (pH 7), multi-layered nanorod petal flowers (pH 8-9), and micro flowers of nanoneedles with pyramid tips (pH 10) were used for degradation of methylene blue (MB) under UV irradiation.[90] Hexagonal ZnO nanoplates degraded 97.54 % MB, much higher than multi-layered nanorod petal flowers (67.27-77.82 %) and micro flowers of nanoneedles with pyramid tips (89.10 %). After the fifth cycle degradation efficiency of hexagonal ZnO nanoplates and ZnO flowers of nanoneedle petals with the hexagonal pyramid, tips were reduced to only 2 %.

3.4 Sensing:

Currently, 2D nanomaterials have considerable interest in the field of the development of reliable sensing systems. 2D nanomaterials sensing elements have numerous advantages over their bulk counterpart. Free-standing 2D nanosheet has a large surface area, providing a more interactive site than the bulk counter. 2D nanosheets have good mechanical stability than 1 and 0 dimensions owing to their scant grain boundaries and effective electron transport.[164-166] Moreover, their tunable chemical and physical properties make these materials promising candidates for sensing applications.[167, 168] ZnO nanosheet has been widely used in sensing applications Owing to its high sensitivity, stability, and low cost.[169, 170] ZnO nonmaterial is mainly used for volatile organic compounds, Nitrogen Dioxide sensing, etc., which are discussed below in detail.

3.4.1 Sensing of Organic Compounds:

Xu and co-workers performed sensing measurements by porous ZnO nanosheets powders with different exposed crystal facets (0001) and (10 $\bar{1}$ 0) by coating terpeneol paste on a ceramic tube with Au electrodes, followed by sintered at 500 °C for 2 h to enhance the stability of the sensor through removing terpeneol.[91] ZnO nanosheet (0001) exhibited a response of 3.9 for 1 ppm ethanol. In contrast, nanosheet (10 $\bar{1}$ 0) showed a 1.4 response for the same amount of ethanol which suggests sensing performance strongly depends on its exposed crystal facet (Figure 12 a). Further, porous ZnO nanosheets showed excellent sensitivity between the different gases such as H₂, NO_x, CO, HCHO, CH₃OH, C₂H₅OH, or NH₃ at an operating temperature of 330 °C (Figure 12 b). ZnO (0001) based sensor maintained excellent stability (80 %) over the ZnO(10 $\bar{1}$ 0) sensor (27.5 %) in 60 days testing period (Figure 12 c). Similarly, a mixture of ZnO hexagonal nanoplate and terpeneol was coated on a ceramic tube and annealed at different temperatures (300, 500, and 700 °C).[80] as shown in (Figure 12 d-e). ZnO-500 shows better

sensitivity towards ethanol at the concentration of 100 ppm than other samples at 340 °C (Figure 12 f). The performance of ZnO-based sensors is increased mainly due to their porous nature, grain size, and Cl element present in the material structure. Further, Ju and co-workers did a comparative study of ZnO-based ethanol sensors by varying reaction times (3 h, 8 h, 12 h) and ethanol concentration.[171] Sensor B (8h) demonstrated a response of 38.4 and 15 for 100 and 25 ppm of ethanol at 400 °C, respectively (Figure 12 g), with excellent selectivity than other gases (Figure 12 h). ZnO nanosheets exhibited high response, fast response-recovery curves, and long-term stability due to the high surface area.

Also, Zhang and co-workers have reported a mesoporous 2D hexagonal ZnO nanosheet which showed a higher response at low ethanol concentration and fast response/recovery times ranging from 0.01-1000 ppm of ethanol at 400 °C.[123] Moreover, it has a detection limit of as low as 10 ppb with a 3.05 response (Figure 12 i). Figure 12 j-k clearly showed the better selectivity of the ZnO sensor for ethanol over the 11 other gases, and high stability at 200 ppm ethanol in 60 days was also displayed. Its large specific surface area mainly causes this with small thickness, single-crystal structure, plane contact between nanosheets, and 3D network architecture.

Further, Xiao and co-workers studied with and without Pd nanoparticles decorated single-crystalline ZnO nanosheet for acetone sensing.[81] The comparative study of response/recovery time of ZnO-nanosheet (NSs) and Pd-ZnO-NSs. The Pd-ZnO-NSs-based sensor yielded ~222 responses toward 500 ppm of acetone which is 3 times higher than the ZnO-NSs-based sensor (Figure 13 a). Additionally, for 100 ppm of ethanol, the response and recovery times of Pd-ZnO-NSs sensors were 9 and 6 s, against 10 and 7 s for ZnO-NSs sensors, respectively. After Pd nanoparticles decoration, the selectivity of ZnO NSs drastically increased (Figure 13 b). In addition, the stability study found that Pd-ZnO-NSs sensors

maintain ~70 % responses. In contrast, ZnO-NSs sensors' responses reduce from 37.5 to 26.5, i.e., 30.4 % at acetone of 100 ppm after 60 days which suggests the enhanced stability and better response of Pd-ZnO-NSs to acetone (Figure 13 c). This high performance was attributed to the specific porous structure of ZnO nanosheets and their surface modification with Pd nanoparticles. In addition, Wang and co-workers have analyzed the sensing properties of naked ZnO, Phosphor (P)-doped ZnO nanosheet, and ZnO nanosheets/graphene oxide (GO) nanocomposites at 240 °C for 50-500 ppm of acetone.[86] All three sensors showed more selectivity to the acetone and ethanol than other gases such as benzene, formaldehyde, methanol, ammonia, carbon monoxide, hydrogen, methane, and iso-butane (Figure 13 d). Figure 13 e is response-recovery characteristic curves, exhibiting 13 s and 7 s response/recovery time for both ZnO/GO and P-doped ZnO nanosheet-based sensor while 13 s and 17 s for the pure ZnO-based sensor (Figure 13 e). This short recovery time might be due to the 2D structure of the material.

Additionally, Wang and co-workers used porous ZnO nanosheets to detect ethylene in the range of 10 ppm to 2000 ppm at 500 °C optimal temperature.[128] As a result, it showed 8 s and 20 s response/recovery time with good selectivity over the different gases (ethyl acetate, acetone, methanol, ethanol, and n-butanol) and long-term stability at higher concentrations of ethylene (2000 ppm) as shown in (Figure 13 f-h). This high response was attributed to the single-crystal structure and porous nanosheet-like morphologies.

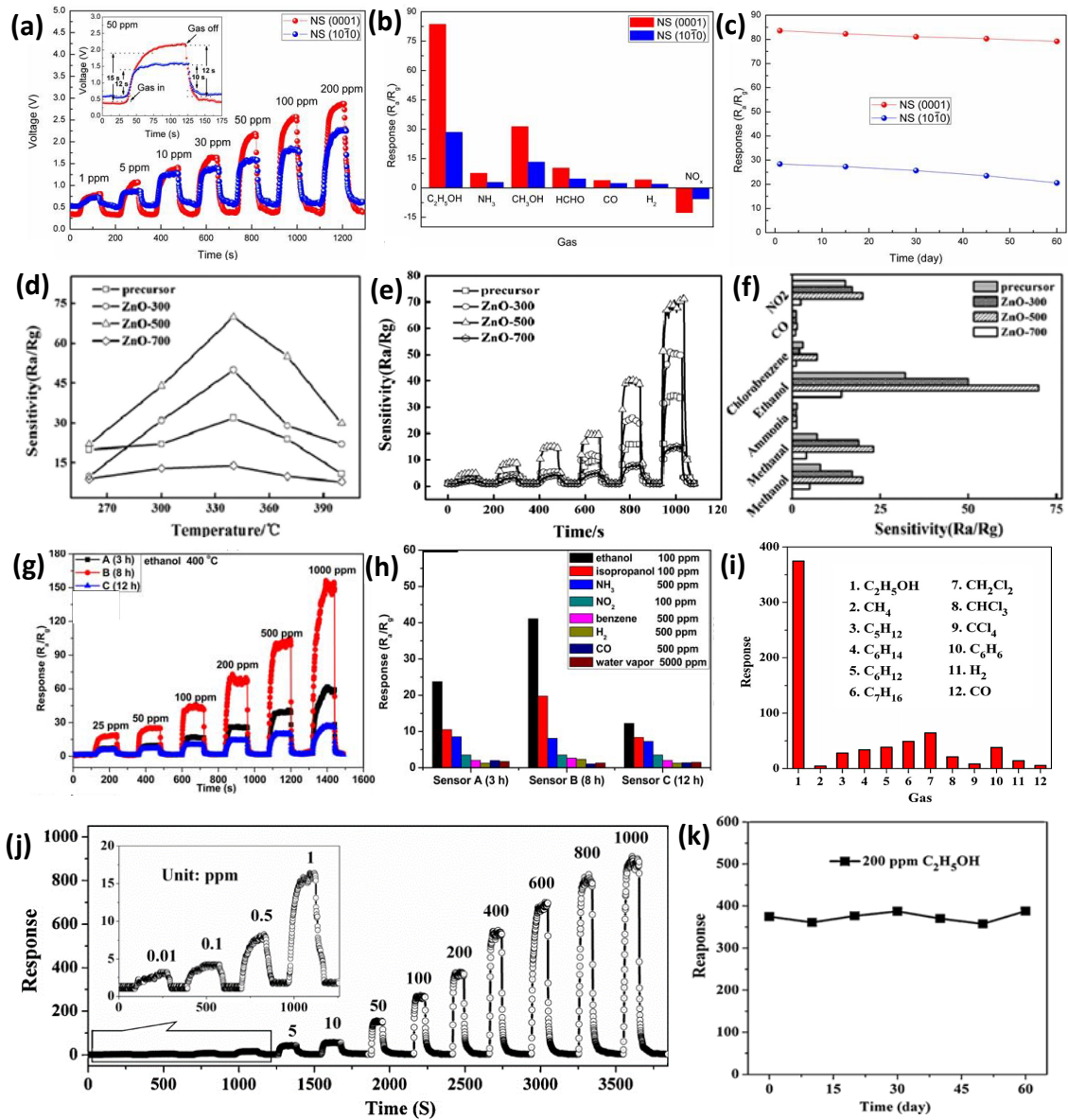


Figure 12. (a) Represent response of ZnO nanosheet sensor with different facets to ethanol vapor of various concentrations. The low concentrated response-recovery curve was magnified as inset (b) selectivity of the sensors to different interfering gases. (c) long-term stability study. “Reprinted from permission [91]. Copyright 2017, Elsevier.” (d-e) Response curve at (d) different operating temperatures (e) different concentrations of ethanol (f) different gases at 100 ppm concentration. “Reprinted from permission [80]. Copyright 2017, Elsevier. Comparative response study between 3 sensors (g) at different ethanol concentrations. (h) different interfering gases. “Reprinted from permission [171]. Copyright 2014, Elsevier.” (i-k)

Response and recovery Vs (i) ethanol concentration, inset is the gas response of the sensors to 0.01-1 ppm. (j) at different interfering gases at 400 °C. (k) stability curve of 200 ppm ethanol concentration at 400 °C. “Reprinted from permission [123]. Copyright 2012, Elsevier.”

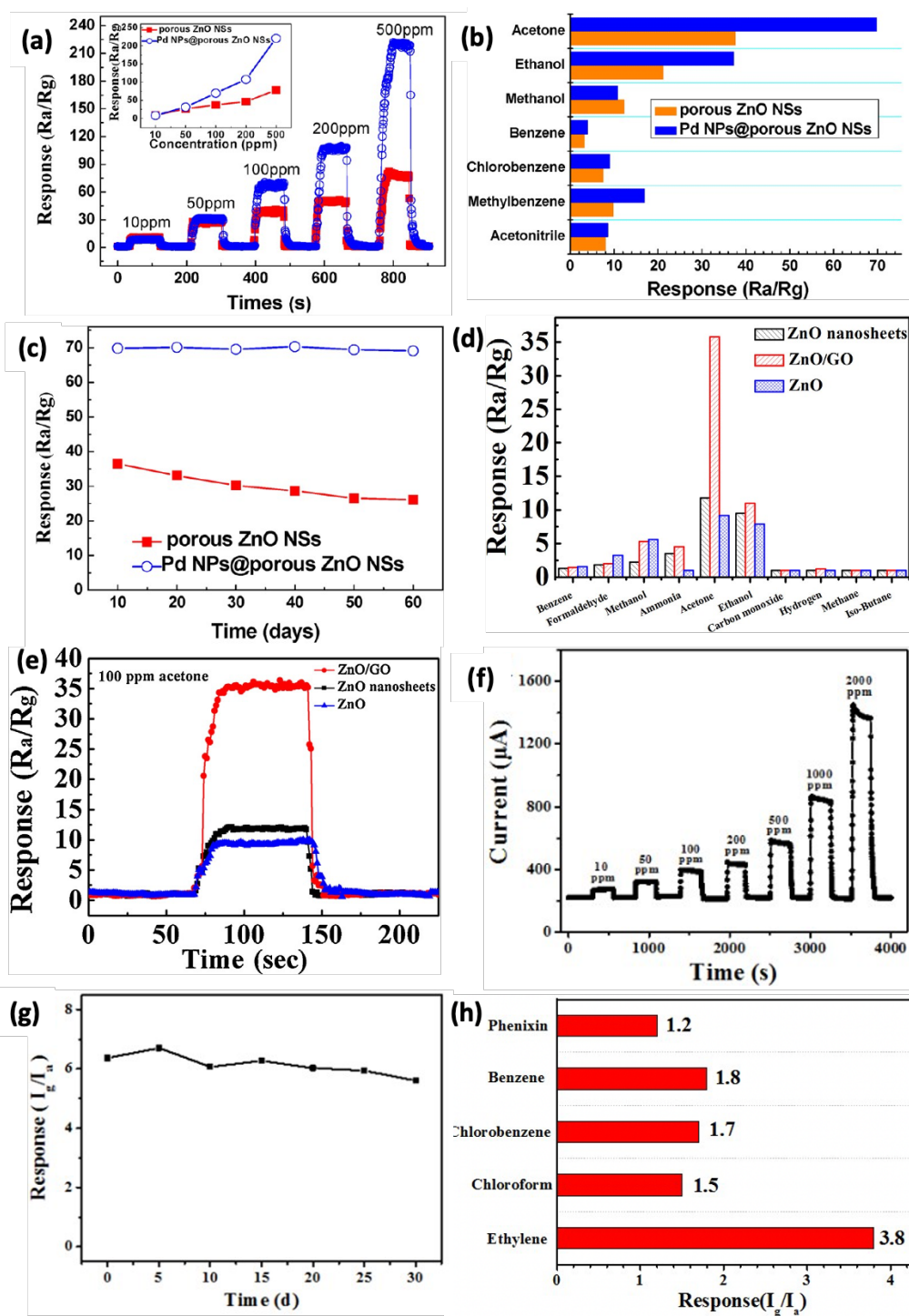


Figure 13. (a) Gas responses of Pd-ZnO-NSs and ZnO-NSs sensors to acetone at concentrations measuring from 10 to 500 ppm. The inset image represented response Vs concentration curves. (b) Acetone selectivity over other interfering gases. (c) Long-term stability study. The sensing performance of pure ZnO, ZnO nanosheets, and ZnO/GO nanocomposites sensors. Reprinted from permission [81]. Copyright 2012, American Chemical Society. (d) Selectivity (e) Sensing characteristics to 100 ppm acetone of 240 °C. “Reprinted from permission [86]. Copyright 2016, Elsevier. The sensing activity of porous ZnO nanosheets. (f) sensing characteristics (g) stability to 2000 ppm of ethylene and (h) response to various gases. Reprinted from permission [128]. Copyright 2019, Royal Society of Chemistry.

3.4.2 Nitrogen Dioxide (NO₂):

In 2011, Chen and co-workers demonstrated that ZnO polygonal nanoflakes could be used for NO₂ sensing.[93] The fabricated sensor shows good selectivity towards the NO₂ at 0.5 ppm over other gaseous at 80 ppm with an operating temperature of 175 °C. The enhanced sensing response was ascribed to crystal defect in the ZnO structure, consisting of oxygen vacancy and interstitial zinc sites. Further, in situ diffuse reflectance infrared Fourier transform spectroscopy technique was used to study surface-adsorbed species on ZnO nanoflakes. This confirmed that nitrate and nitrite anions were the primary adsorbed species on the surface of ZnO. ZnO nanosheet or nanowall having a lesser thickness than ZnO nanoflake, leading to enhanced sensing performance (higher sensitivity, faster response/recovery, and lower operation temperature).[172] Yu and co-workers explored the ZnO nanowall-based sensor for NO₂ sensing in the broad range of 1-50 ppm at the optimal temperature of 220 °C (Figure 14 a).[94] It showed sensitivity (S=30) to 50 ppm of NO₂ (Figure 14 b) with fast response and recovery times of 30 and 48 s, respectively (Figure 14 c). Further, the author studied the sensing

performance of annealed ZnO nanowalls at a different temperature from 350-750 °C for 1 h. [95] Figure 14 d demonstrates the response of annealed ZnO nanowalls from 350 to 450 °C towards NO₂ with a gradually increased concentration of 50 ppm. After raising the reaction temperature (500 to 750 °C), gas response towards the NO₂ decreased, confirming that 450 °C is an ideal operating temperature for NO₂ sensing. The gas sensitivity of the sensor was enhanced while increasing the NO₂ concentration, as shown in Figure 14 e. it showed a high response (6.4) at a 50-ppm concentration of NO₂. Figure 14 f shows good stability after 3 cycles attributed to the enhanced porosity and oxygen vacancies. Similarly, Xiao and co-workers reported ZnO nanosheets with exposed (100) facets that could detect NO₂ at lower temperatures ranging from 120 to 240 °C as compared to the previous study (Figure 14 g).[173] At 180 °C operating temperature, it showed a high response toward 100 ppm NO₂ (Figure 14 h). Further, the response at different concentration ranges of 1-400 ppm at 180 °C was studied. The resulting sensor showed that the response and recovery times for NO₂ at 10 ppm were 3 and 12 s, respectively, with excellent selectivity than other gases (H₂S, ethanol, benzene, acetone, methanol, methanol, toluene, and NH₃) (Figure 14 i). The high gas sensing performance was attributed to the abundant oxygen vacancies on the (100) exposed surfaces, which act as active sites for NO₂ adsorption.

Moreover, Mun and co-workers reported sensing properties of Au-functionalized ZnO nanosheets over pristine ZnO nanosheets under UV irradiation (1.2 mW/cm²).[174] Au-functionalized ZnO nanosheets exhibited high response (~205 to ~455 %) than pristine ZnO nanosheets (~111 to ~137 %) in the range of 1 to 5ppm at room temperature (Figure 14 j). Also, the Au-functionalized ZnO nanosheet demonstrated good selectivity (Figure 14 k) to NO₂ gas over other gases such as CO, H₂S, and C₂H₅OH than pristine ZnO nanosheet.

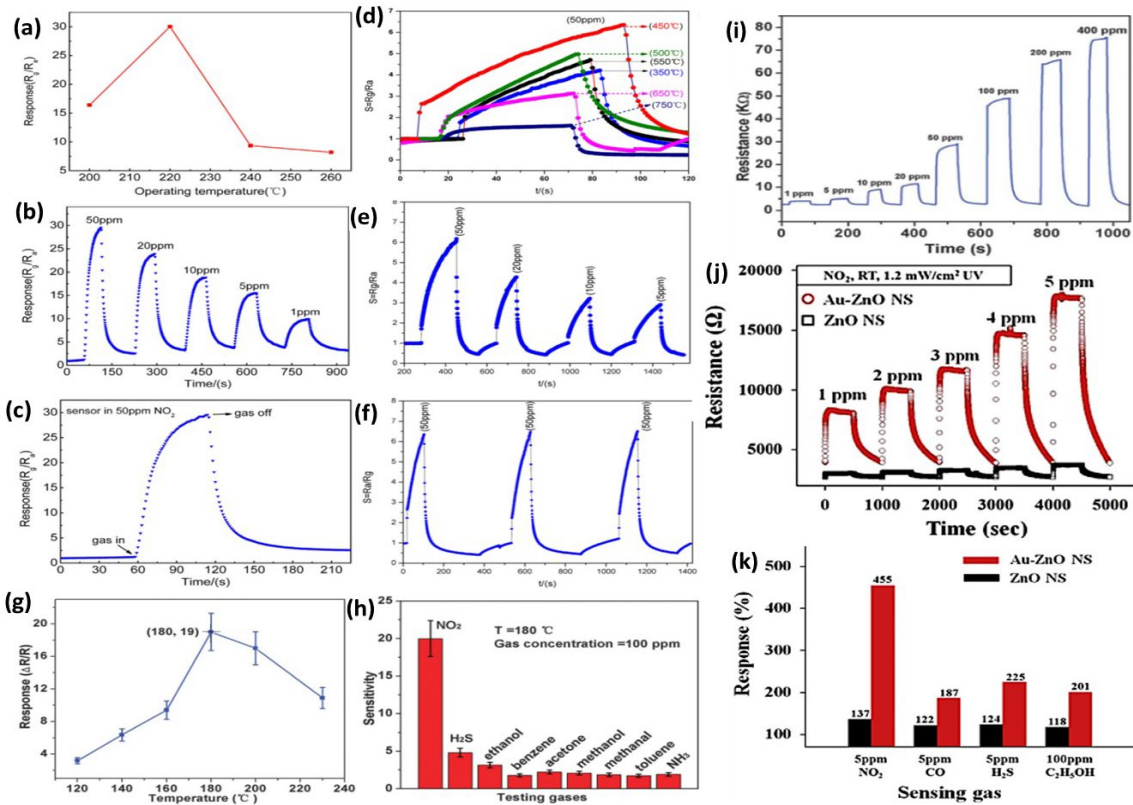


Figure 14. (a-b) The response curve of (a) 50 ppm NO_2 at different temperatures, (b) different concentrations of NO_2 (c) response–recovery curve at 50 ppm NO_2 concentration. “Reprinted from permission [94]. Copyright 2014, Elsevier.” (d-f) Sensitivity plot of ZnO nanowall-based sensor (d) at the different annealing temperatures. (e) at different NO_2 concentrations. (f) stability study at 50 ppm NO_2 . “Reprinted from permission [95]. Copyright 2016, Elsevier.” (g-i) Response curve (g) at different temperatures (h) at different concentrations. (i) selectivity over other interfering gases. “Reprinted from permission [173]. Copyright 2016, Royal Society of Chemistry.” Response of (j) pristine and Au-functionalized ZnO nanosheets at 1-5 ppm NO_2 gas, (k) selectivity. “Reprinted from permission [174]. Copyright 2013, Elsevier.”

3.5 Piezotronics and piezo-phototronics:

There is a ubiquitous and abundant source of mechanical triggering signals in the environment, such as vibration and biological moments, and it can power and control the nanodevices. The sensors are conventionally used to detect and record mechanical stimuli. However, they cannot control electronics further, which is known as passive electronics. Therefore, the direct interaction of mechanical stimuli with current electronic technologies is crucial for human-machine interfacing. Piezotronics and piezo-phototronics have potential applications in the field comprising electronics-human/ambience interaction, such as human-machine interfacing, biomedical engineering, smart skin, and robotics. In principle, piezoelectronics couples piezoelectricity with semiconducting properties of materials by piezoelectric polarization charges induced by stress/strain, and piezo-phototronics couples photons with piezoelectricity and third-generation semiconductors.[71, 175-177] A gate-controlling signal generated by the piezoelectric polarization can be used to design intelligent electronic devices.[96] The piezotronic effect is mainly observed in wurtzite crystal structure semiconductors such as ZnO.[178-181] Induced piezopotential act as a 'gate' controlling signal tunes the barrier present at the interface and finally controls the transport of free charge carriers. This technique controls electronic devices by producing digital signals without using any additional source.

Wang and co-workers studied 2D piezotronics in ultrathin ZnO nanosheets. Notably, 2D ZnO nanosheet showed a high piezoelectric coefficient (d_{eff}) ($\sim 21.5 \pm 1.5$ pm./V) as compared to other 2D materials. [182-184] 2D ZnO nanosheet has a large surface area. Additionally, defects present at the surface of the ZnO nanosheet give polarization and low carrier capability, enhancing the device's piezoelectric coefficient.[166, 185] To study the electrical transport properties of a ZnO, by varying the stress on the two-terminal electronic devices, authors designed ZnO sandwiched between metal and packed with polymethyl methacrylate (PMMA)

polymer (Figure 15 a). Figure 15 b demonstrates that free carrier transportation gradually increases while increasing the stress on a device. The external force was applied to the electrodes to study the interfacing gating effect. Typically, negative piezo potential attracts holes and lower Schottky barriers of the metal-ZnO contacts.

Consequently, this enhances the transport conductance of the devices (Figure 15 c). ZnO's electrical transport properties were studied at different pressures to investigate the pressure effects on the electronic structure. With increasing pressure, the current increased steadily, indicating an increase in the Schottky barrier (Figure 15 d). Further, Schottky barrier height (SBH) showed linear relation towards compressed pressure which shows SBH tuned by stress-induced out-of-plane piezo potential (Figure 15 e). Further, to understand the channel width gating effect, the external force was applied to the channel of the manufactured device. Distributed hole concentrations along the direction of the c-axis at different strains were assured concentration. The dispersion of free carriers in the nanosheet was affected by stress-induced piezoelectric polarization charges (Figure 15 f).

Additionally, the width of the conductive channel is moderated by stress-induced out-of-plane piezo potential (Figure 16 a). Here, mechanical stress act as a controlling gate signal and modulate the transport properties of 2D piezotronic devices, which reduces the conducting channel by preparing the depletion region and enhances the resistance of ZnO (Figure 16 b). A series of mechanical strains were given to the piezotronic devices with back-to-back Schottky barriers to understand the effect of interfacing gates in different thicknesses. The electrical transport characteristics of the device at various thicknesses were studied Figure 16 c shows a remarkable change in SBH as the thickness of the nanosheet decreased. The device's sensitivity was increased, ranging from 900 ± 5.83 meV to 1331.77 ± 8.53 meV while decreasing the

thickness of the nanosheet from 100 nm to 2 nm. The concentration of holes reduces quickly with increasing the depletion region width at 100 nm thickness.

Moreover, the screening effect of the carrier of ultrathin ZnO nanosheet (<10 nm) was remarkably decreased because of the low hole concentration, as shown in Figure 16 d. Consequently, negative piezoelectric polarization charges are generated at the interface of metal ZnO. It concluded that when a negative piezoelectric charge was applied to the device Schottky barrier was tuned significantly, and the effect of the interfacing gate increased with decreasing ZnO nanosheet thickness (Figure 16 e). Further, the channel-width gating effect width as a function of the thickness of the nanosheet was studied by applying modulated strain on electric transport characteristics. The device's output current suppressed upon applying more strain to a piezotronic device. It acts like a diode, meaning applied stain control and modulated transportation of charge carriers. Figure 16 g revealed that the channel width gating effect significantly reduced the thickness.

Further, Chun Hua and co-workers prepared the device by assembling deposited ultrathin ZnO nanosheet on SiO/Si substrate, Au electrode and packed with PMMA polymer (Figure 16 h).[186] To study the electrical transport characteristics of the device, a series of pressure was applied at metal-semiconductor contact (Figure 16 i). Output current increased remarkably with increasing the pressure ranging from 0-5.3 MPa, which confirmed at nanoscale piezo-phototronic effect was more significant and played a crucial role in photo-induced charge carriers transport characteristics. Figure 16 j shows the photoresponsivity curve of a ZnO-based device with bias voltage -2 V. Photoresponsivity curve initially increased monotonically till 3 MPa and then saturated moderately. It showed 1.45×10^3 A/W photoresponsivity at $10 \mu\text{W}/\text{cm}^2$ and 5.3 MPa power intensity and pressure, respectively, which is 230 % higher photoresponsivity than pressure-free photoresponsivity with 1000 times higher compared to

other commercially available ultraviolet photodetectors (0.1 - 0.2 A/W). It reveals that ZnO nanosheets open the doorways toward piezotronic and piezo-phototronic devices due to their ultrathin thickness and strong out-of-plane piezoelectricity.

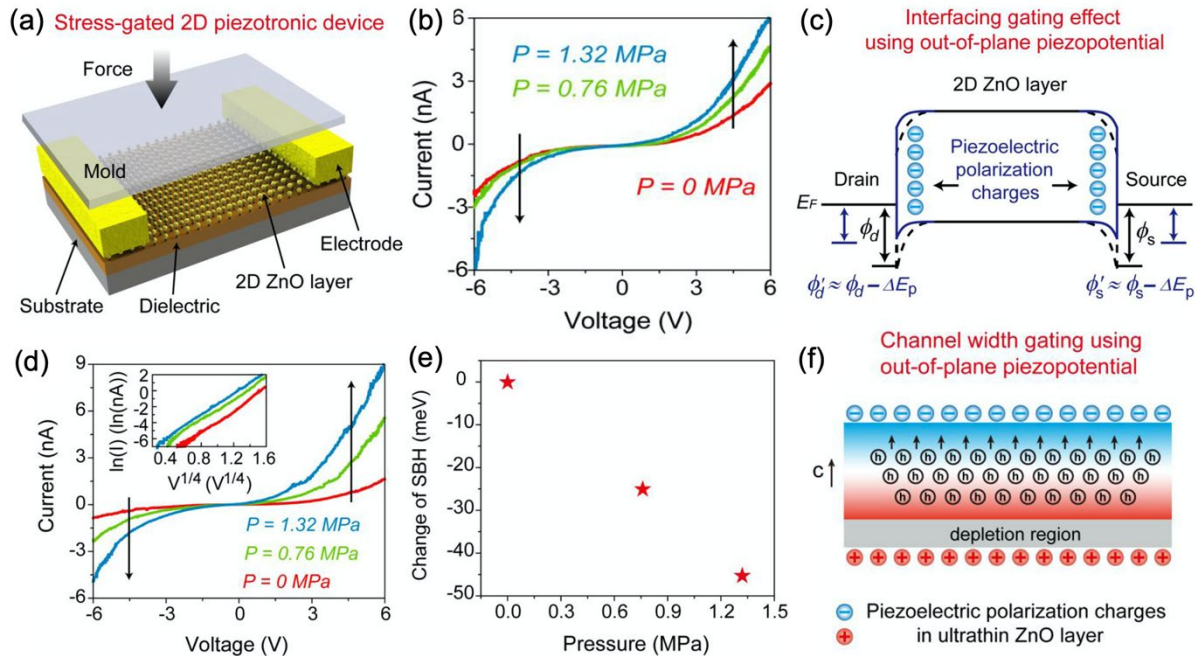


Figure 15. (a,) Schematic diagram of fabricated 2D ZnO-based piezotronic device. (b,d) Charge transport characteristic curve at series of applied (b) stress (d) pressure. (c) Band diagram of ZnO nanosheet while negative piezoelectric polarization charges at interface. (e) The plot of change of SBH Vs applied pressures. (f) Schematic representation of hole distribution in nanosheet. “Reprinted from permission [96]. Copyright 2019, Elsevier.”

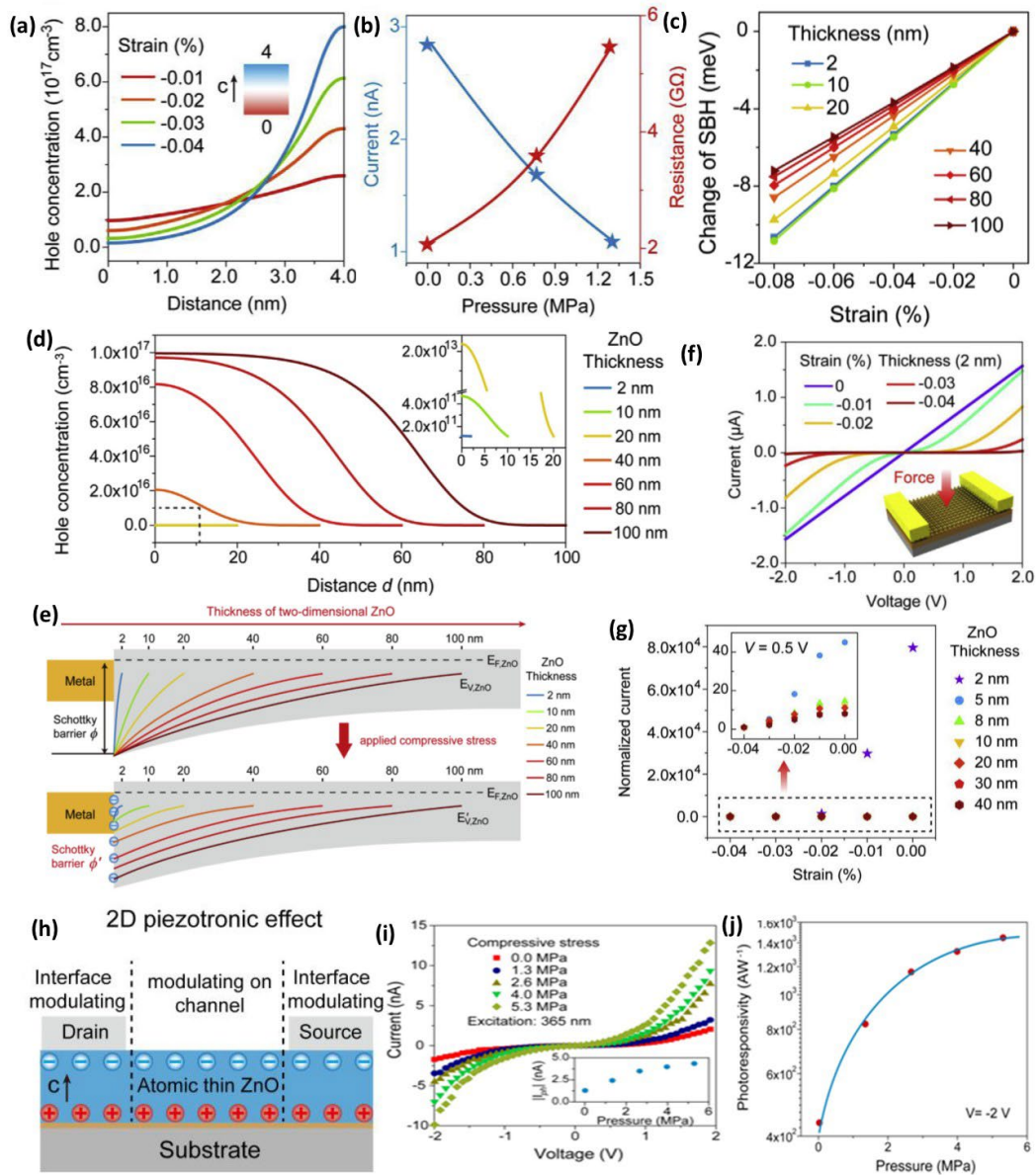


Figure 16. (a-b) Effect of the width of channel gate in the device (a) holes distribution at different strain values. (b) The plot of current and resistivity at different pressure. (c) The plot of SBH as a function of thickness. (d) Hole concentration distribution under strain-free conditions. (e) Band diagram. (f-g) thickness dependence effect of the width of channel gate (f) characteristic curve of electrical transport properties. (g) The plot of normalized current Vs strain at different thicknesses. “Reprinted from permission [96]. Copyright 2019, Elsevier.” (h) Schematic diagram of fabricated 2D ZnO-based piezotronic device. (i) the characteristic curve of electrical transport properties at different applied pressure. (j) The plot of photoresponsivity

as a function of applied pressures. “Reprinted from permission [186]. Copyright 2021, Elsevier.”

5. Summary and prospects:

Over the last few decades, incredible research has been developed in ultrathin 2D nanomaterials. In this review, we have focused on the synthesis strategies, including ILE, CVD, 2D-templated synthesis, solvothermal synthesis, self-assembly, and 2D-oriented attachment, which have advantages. The thickness, size, surface properties, and crystallinity of the 2D ZnO nanostructures depend upon the synthesis method, which is beneficial for different applications. From the synthesis point of view, there are some challenges in the wet chemical synthesis method. (a) it is hard to synthesize monolayer nanostructure. (b) the lateral size of the nanostructure is less than 1 μm . In addition, the surfactant-based methods demonstrate a promising synthesis method for free-standing, large-area 2D ZnO nanostructures, which are beneficial in device fabrication with complex components. Further, enhancing the production rate of nanomaterials to compete with commercial sources is also one major challenge for academic researchers.

From the application point of view, ZnO nanostructures act as an electrode material and show potential application in energy storage devices due to their high theoretical capacity, high electrical conductivity, and large surface area. Moreover, it also showed photocatalytic activity as a result of oxygen defects, the morphology of the nanostructures, and orientation.

Further, ZnO-based nanostructures are used in sensing applications. The donor defect level in n-type ZnO semiconductors is dominant. Defects present on the surface enhance the adsorption sites on the ZnO surface, which strengthens the redox reaction efficiency resulting in effects on the sensing properties of ZnO-based nanomaterials. Improving the sensitivity,

selectivity, and stability and reducing the ZnO-based sensor's response /recovery time are significant challenges in sensing applications. In addition, humidity condition influences the sensing properties of ZnO-based sensor. In lab-scale sensing, the study was performed in a controlled environment. However, at the industrial level, humidity changes continuously. Hence, it is imperative to study the sensitivity at various humidity conditions.

Moreover, the direct deposition of ZnO material on the electrode reduces the morphology destruction, which gives a high surface area and an effective charge carrier transport channel. Consequently, enhance the performance of ZnO-based sensor. Furthermore, 2D nanostructures are widely used in optoelectronic devices due to their unique properties, such as wide bandgap, large exciton bandgap energy (60 meV), and high breakdown voltage. Nevertheless, there are some unsolved issues. For example, responsivity, sensitivity and response speed, stability, durability, eco-friendly and cost-effective processing. Apart from this, mass production and designing complex circuits in a small area are significant challenges for future research.

Above mentioned synthesis strategies for 2D ZnO nanostructures might be helpful in the research in van der Waals heterostructures for the possibility of real-time applications as currently Van der Waals heterostructures are prepared by exfoliation methods that have limitations due to small lateral size/area. The synthesis of wrinkle-free 2D nanosheets by optimizing reaction time, surface pressure, precursor concentrations, use of proper amphiphilic molecules, and surface reduction chemistry might significantly impact the basic to applied research in the field.

6. Abbreviation

1D	1-Dimensional	Å	Angstrom
2D	2-Dimensional	A-L-S	Air-liquid-solid

AFM	Atomic Force Microscopy	ILE	Ionic Layer Epitaxy
Al ₂ O ₃	Aluminum oxide	LB	Langmuir-Blodgett
ALD	Atomic layer deposition	LEDs	Light emitting diode
AO7	Acid orange 7	LIBs	Lithium-ion batteries
CBD	Chemical bath deposition	MB	Methylene blue
CHCl ₃	Chloroform	MD	Molecular dynamics
CVD	Chemical Vapour Deposition	MO	Methyl orange
d	Lattice distance	Na ⁺	Sodium hydrated ion
d _{eff}	Piezoelectric coefficient	NaOH	Sodium hydroxide
DS ⁻	Dodecyl sulfate ions	NBED	Nano beam electron diffraction
EG	Ethylene Glycol	NFs	Nanoflowers
eV	Electron volt	NH ₄ F	Ammonium fluoride
FESEM	Field Emission Scanning Electron Microscopy	NH ₄ HCO ₃	Ammonium hydrogen carbonate
FETs	Field-effect transistors	nm	Nanometer
FFT	Fast Fourier Transfer	NMs	Nanomembranes
GO	Graphene oxide	NPs	Nanoparticles
GZL	Grid-like ZnO lamellae	NSs	Nanosheets
gZnO	Graphitic ZnO	OAM	Oleylamine
HCl	Hydrogen chloride	P(St-MMA-SPMAP)	Poly(styrene-methyl methacrylate-sulfo propyl methacrylate potassium)
HMTA	Hexamethylenetetramine	P ₂ O ₅	Phosphor pentoxide
HRTEM	High Resolution Transmission Electron Microscopy	PFM	Piezoresponse force microscopy
I _D	Drain current	PL	Photoluminescence
I _G	Gate current		

PMMA	Polymethyl methacrylate	VS	Vapor solid
PVP	Polyvinylpyrrolidone	ZHDS	Zinc hydroxide dodecyl sulfate
QDs	Quantum dots		
rGO	Reduced graphene oxide	ZHS	Zinc hydroxy sulfate
RhB	Rhodamine B	$\text{Zn}(\text{NO}_3)_2$	Zinc nitrate
SAED	Selected Area Electron Diffraction	$\text{Zn}(\text{NO}_3)_2 \cdot 6\text{H}_2\text{O}$	Zinc nitrate hexahydrate
SBH	Schottky barrier height	$\text{Zn}(\text{OH})_4$	Zinc hydroxide
SDBS	Sodium dodecyl benzene sulfonate	$\text{Zn}_5(\text{CO}_3)_2(\text{OH})_6$	Hydrozincite
SDS	Sodium dodecyl sulfate	$\text{Zn}_5(\text{OH})_8\text{Cl}_2$	Zinc chloride hydroxide monohydrate
SEM	Scanning Electron Microscopy	$\text{Zn}_5(\text{OH})_8\text{Cl}_2 \cdot \text{H}_2\text{O}$	Zinc chloride hydroxide monohydrate
SILAR	Successive Ionic Layer Adsorption and Reaction	ZnCl_2	Zinc chloride,
SiO_2/Si	Oxide-coated Si substrates	Zn_{is}	Zinc interstitials
SOS	Sodium oleyl sulfate	ZnO	Zinc oxide
TEM	Transmission Electron Microscopy	ZnO (pa)	Zinc oxide n-propylamine
TMOs	Transition metal oxides	ZnO -MSN	Zinc oxide mesoporous single crystal nanosheet
UV	Ultra violet	ZnS (pa)	Zinc sulfate n-propylamine
V_D	Drain voltage	ZnSO_4	Zinc sulphate
V_G	Gate voltage	μm	Micrometer
V_{os}	Oxygen vacancies		

Notes

† SAP and PBJ contributed equally.

Conflicts of interest

There are no conflicts to declare.

7. Acknowledgements:

SAP thanks SERB for junior research fellowship. RVS and AS acknowledge R & D Merck India for providing the infrastructure. ZK acknowledges Åforsk foundation for project anode free Zn-ion battery (21-130). SAP, PBJ and MS acknowledge funding support from SERB, New Delhi (EMR/2017/003368).

8. References:

1. Tan, C.; Cao, X.; Wu, X.-J.; He, Q.; Yang, J.; Zhang, X.; Chen, J.; Zhao, W.; Han, S.; Nam, G.-H., *Chem. Rev.* **2017**, *117* (9), 6225-6331.
2. Gong, C.; Hu, K.; Wang, X.; Wangyang, P.; Yan, C.; Chu, J.; Liao, M.; Dai, L.; Zhai, T.; Wang, C., *Adv. Funct. Mater.* **2018**, *28* (16), 1706559.
3. Radisavljevic, B.; Radenovic, A.; Brivio, J.; Giacometti, V.; Kis, A., *Nat. Nanotechnol.* **2011**, *6* (3), 147-150.
4. Yin, Z.; Li, H.; Li, H.; Jiang, L.; Shi, Y.; Sun, Y.; Lu, G.; Zhang, Q.; Chen, X.; Zhang, H., *ACS Nano* **2012**, *6* (1), 74-80.
5. Liang, L.; Li, K.; Xiao, C.; Fan, S.; Liu, J.; Zhang, W.; Xu, W.; Tong, W.; Liao, J.; Zhou, Y., *J. Am. Chem. Soc.* **2015**, *137* (8), 3102-3108.
6. Song, F.; Hu, X., *Nat. Commun.* **2014**, *5* (1), 1-9.
7. Voiry, D.; Yamaguchi, H.; Li, J.; Silva, R.; Alves, D. C.; Fujita, T.; Chen, M.; Asefa, T.; Shenoy, V. B.; Eda, G., *Nat. Mater.* **2013**, *12* (9), 850-855.
8. Yang, S.; Gong, Y.; Zhang, J.; Zhan, L.; Ma, L.; Fang, Z.; Vajtai, R.; Wang, X.; Ajayan, P. M., *Adv. Mater.* **2013**, *25* (17), 2452-2456.
9. Du, G.; Guo, Z.; Wang, S.; Zeng, R.; Chen, Z.; Liu, H., *ChemComm* **2010**, *46* (7), 1106-1108.
10. Tsai, M.-L.; Su, S.-H.; Chang, J.-K.; Tsai, D.-S.; Chen, C.-H.; Wu, C.-I.; Li, L.-J.; Chen, L.-J.; He, J.-H., *ACS Nano* **2014**, *8* (8), 8317-8322.
11. Zhu, C.; Zeng, Z.; Li, H.; Li, F.; Fan, C.; Zhang, H., *J. Am. Chem. Soc.* **2013**, *135* (16), 5998-6001.
12. Perkins, F. K.; Friedman, A. L.; Cobas, E.; Campbell, P.; Jernigan, G.; Jonker, B. T., *Nano Lett.* **2013**, *13* (2), 668-673.
13. Cheng, L.; Liu, J.; Gu, X.; Gong, H.; Shi, X.; Liu, T.; Wang, C.; Wang, X.; Liu, G.; Xing, H., *Adv. Mater.* **2014**, *26* (12), 1886-1893.
14. Kim, K. K.; Hsu, A.; Jia, X.; Kim, S. M.; Shi, Y.; Hofmann, M.; Nezich, D.; Rodriguez-Nieva, J. F.; Dresselhaus, M.; Palacios, T., *Nano Lett.* **2012**, *12* (1), 161-166.
15. Lin, Y.; Williams, T. V.; Connell, J. W., *J. Phys. Chem. Lett.* **2010**, *1* (1), 277-283.
16. Song, L.; Ci, L.; Lu, H.; Sorokin, P. B.; Jin, C.; Ni, J.; Kvashnin, A. G.; Kvashnin, D. G.; Lou, J.; Yakobson, B. I., *Nano Lett.* **2010**, *10* (8), 3209-3215.
17. Weng, Q.; Wang, X.; Wang, X.; Bando, Y.; Golberg, D., *Chem. Soc. Rev.* **2016**, *45* (14), 3989-4012.
18. Chhowalla, M.; Shin, H. S.; Eda, G.; Li, L.-J.; Loh, K. P.; Zhang, H., *Nat. Chem.* **2013**, *5* (4), 263-275.
19. Huang, X.; Zeng, Z.; Zhang, H., *Chem. Soc. Rev.* **2013**, *42* (5), 1934-1946.
20. Lopez-Sanchez, O.; Lembke, D.; Kayci, M.; Radenovic, A.; Kis, A., *Nat. Nanotechnol.* **2013**, *8* (7), 497-501.
21. Lv, R.; Robinson, J. A.; Schaak, R. E.; Sun, D.; Sun, Y.; Mallouk, T. E.; Terrones, M., *Acc. Chem. Res.* **2015**, *48* (1), 56-64.
22. Zhang, J.; Chen, Y.; Wang, X., *Energy Environ. Sci.* **2015**, *8* (11), 3092-3108.
23. Ong, W.-J.; Tan, L.-L.; Ng, Y. H.; Yong, S.-T.; Chai, S.-P., *Chem. Rev.* **2016**, *116* (12), 7159-7329.
24. Osada, M.; Sasaki, T., *J. Mater. Chem.* **2009**, *19* (17), 2503-2511.
25. Ma, R.; Sasaki, T., *Acc. Chem. Res.* **2015**, *48* (1), 136-143.
26. Lv, L.; Yang, Z.; Chen, K.; Wang, C.; Xiong, Y., *Adv. Energy Mater.* **2019**, *9* (17), 1803358.
27. Liu, H.; Du, Y.; Deng, Y.; Peide, D. Y., *Chem. Soc. Rev.* **2015**, *44* (9), 2732-2743.
28. Eswaraiiah, V.; Zeng, Q.; Long, Y.; Liu, Z., *Small* **2016**, *12* (26), 3480-3502.

29. Lalmi, B.; Oughaddou, H.; Enriquez, H.; Kara, A.; Vizzini, S.; Ealet, B.; Aufray, B., *Appl. Phys. Lett.* **2010**, *97* (22), 223109.
30. Vogt, P.; De Padova, P.; Quaresima, C.; Avila, J.; Frantzeskakis, E.; Asensio, M. C.; Resta, A.; Ealet, B.; Le Lay, G., *Phys. Rev. Lett.* **2012**, *108* (15), 155501.
31. Tao, L.; Cinquanta, E.; Chiappe, D.; Grazianetti, C.; Fanciulli, M.; Dubey, M.; Molle, A.; Akinwande, D., *Nat. Nanotechnol.* **2015**, *10* (3), 227-231.
32. Zhang, S.; Yan, Z.; Li, Y.; Chen, Z.; Zeng, H., *Angew. Chem.* **2015**, *127* (10), 3155-3158.
33. Ares, P.; Aguilar-Galindo, F.; Rodríguez-San-Miguel, D.; Aldave, D. A.; Díaz-Tendero, S.; Alcamí, M.; Martín, F.; Gómez-Herrero, J.; Zamora, F., *Adv. Mater.* **2016**, *28* (30), 6332-6336.
34. Singh, D.; Gupta, S. K.; Sonvane, Y.; Lukačević, I., *J. Mater. Chem. C* **2016**, *4* (26), 6386-6390.
35. Wang, Y.; Zhang, Z.; Mao, Y.; Wang, X. J. E.; Science, E., *Energy Environ. Sci.* **2020**, *13* (11), 3993-4016.
36. Dou, Y.; Zhang, L.; Xu, X.; Sun, Z.; Liao, T.; Dou, S. X. J. C. S. R., *Chem. Soc. Rev.* **2017**, *46* (23), 7338-7373.
37. Hu, X.; Liu, K.; Cai, Y.; Zang, S.-Q.; Zhai, T. J. S. S., *Small Sci.* **2022**, *2* (8), 2200008.
38. Leonardi, S. G., *Chemosensors* **2017**, *5* (2), 17.
39. Laurenti, M.; Porro, S.; Pirri, C. F.; Ricciardi, C.; Chiolerio, A., *Crit. Rev. Solid State Mater. Sci.* **2017**, *42* (2), 153-172.
40. Barpuzary, D.; Khan, Z.; Vinothkumar, N.; De, M.; Qureshi, M. J. T. J. o. P. C. C., *J. Phys. Chem. C* **2012**, *116* (1), 150-156.
41. Li, L.; Zhai, T.; Bando, Y.; Golberg, D., *Nano Energy* **2012**, *1* (1), 91-106.
42. Theerthagiri, J.; Salla, S.; Senthil, R.; Nithyadharseni, P.; Madankumar, A.; Arunachalam, P.; Maiyalagan, T.; Kim, H.-S., *Nanotechnology* **2019**, *30* (39), 392001.
43. Yu, S. H.; Yoshimura, M. J. A. M., *Adv. Mater.* **2002**, *14* (4), 296-300.
44. Park, J.-H.; Choi, H.-J.; Choi, Y.-J.; Sohn, S.-H.; Park, J.-G. J. J. o. M. C., *J. Mater. Chem.* **2004**, *14* (1), 35-36.
45. Fu, M.; Zhou, J. J. J. o. t. E. S., *J. Electrochem. Soc.* **2010**, *157* (8), D450.
46. Fan, H. J.; Scholz, R.; Kolb, F. M.; Zacharias, M. J. A. p. l., *Appl. Phys. Lett.* **2004**, *85* (18), 4142-4144.
47. Hosono, E.; Fujihara, S.; Honma, I.; Zhou, H. J. A. M., *Adv. Mater.* **2005**, *17* (17), 2091-2094.
48. Yu, J.; Li, J.; Zhang, W.; Chang, H., *Chem. Sci.* **2015**, *6* (12), 6705-6716.
49. Zhang, Y.; Zhang, L.; Zhou, C., *Acc. Chem. Res.* **2013**, *46* (10), 2329-2339.
50. Reina, A.; Jia, X.; Ho, J.; Nezich, D.; Son, H.; Bulovic, V.; Dresselhaus, M. S.; Kong, J., *Nano Lett.* **2009**, *9* (1), 30-35.
51. Li, X.; Cai, W.; An, J.; Kim, S.; Nah, J.; Yang, D.; Piner, R.; Velamakanni, A.; Jung, I.; Tutuc, E., *science* **2009**, *324* (5932), 1312-1314.
52. Lee, Y. H.; Zhang, X. Q.; Zhang, W.; Chang, M. T.; Lin, C. T.; Chang, K. D.; Yu, Y. C.; Wang, J. T. W.; Chang, C. S.; Li, L. J., *Adv. Mater.* **2012**, *24* (17), 2320-2325.
53. Sun, J.; Lu, C.; Song, Y.; Ji, Q.; Song, X.; Li, Q.; Zhang, Y.; Zhang, L.; Kong, J.; Liu, Z., *Chem. Soc. Rev.* **2018**, *47* (12), 4242-4257.
54. Ji, Q.; Zhang, Y.; Zhang, Y.; Liu, Z., *Chem. Soc. Rev.* **2015**, *44* (9), 2587-2602.
55. Bae, S.; Kim, H.; Lee, Y.; Xu, X.; Park, J.-S.; Zheng, Y.; Balakrishnan, J.; Lei, T.; Kim, H. R.; Song, Y. I., *Nat. Nanotechnol.* **2010**, *5* (8), 574.
56. Han, J. H.; Lee, S.; Cheon, J., *Chem. Soc. Rev.* **2013**, *42* (7), 2581-2591.
57. Tan, C.; Zhang, H., *Nat. Commun.* **2015**, *6* (1), 1-13.
58. Lhuillier, E.; Pedetti, S.; Ithurria, S.; Nadal, B.; Heuclin, H.; Dubertret, B., *Acc. Chem. Res.* **2015**, *48* (1), 22-30.
59. Wu, Y.; Yuan, B.; Li, M.; Zhang, W.-H.; Liu, Y.; Li, C., *Chem. Sci.* **2015**, *6* (3), 1873-1878.
60. Son, J. S.; Yu, J. H.; Kwon, S. G.; Lee, J.; Joo, J.; Hyeon, T., *Adv. Mater.* **2011**, *23* (28), 3214-3219.
61. Qian, X.; Shen, S.; Liu, T.; Cheng, L.; Liu, Z., *Nanoscale* **2015**, *7* (14), 6380-6387.
62. Zhang, H.; Savitzky, B. H.; Yang, J.; Newman, J. T.; Perez, K. A.; Hyun, B.-R.; Kourkoutis, L. F.; Hanrath, T.; Wise, F. W., *Chem. Mater.* **2016**, *28* (1), 127-134.
63. Cheng, L.; Yuan, C.; Shen, S.; Yi, X.; Gong, H.; Yang, K.; Liu, Z., *ACS Nano* **2015**, *9* (11), 11090-11101.
64. Dong, R.; Zhang, T.; Feng, X., *Chem. Rev.* **2018**, *118* (13), 6189-6235.
65. Djurišić, A. B.; Chen, X.; Leung, Y. H.; Ng, A. M. C. J. J. o. M. C., *J. Mater. Chem.* **2012**, *22* (14), 6526-6535.
66. Mishra, Y. K.; Adelung, R. J. M. T., *Mater. Today* **2018**, *21* (6), 631-651.
67. Kumar, B.; Kim, S.-W. J. N. E., *Nano Energy* **2012**, *1* (3), 342-355.
68. Wang, F.; Seo, J.-H.; Luo, G.; Starr, M. B.; Li, Z.; Geng, D.; Yin, X.; Wang, S.; Fraser, D. G.; Morgan, D., *Nat. Commun.* **2016**, *7* (1), 1-7.
69. Tian, H.; Wang, X.; Zhu, Y.; Liao, L.; Wang, X.; Wang, J.; Hu, W., *Appl. Phys. Lett.* **2017**, *110* (4), 043505.
70. Miao, J.; Chen, C.; Meng, L.; Lin, Y., *ACS Sens.* **2019**, *4* (5), 1279-1290.
71. Wu, W.; Wang, Z. L., *Nat. Rev. Mater.* **2016**, *1* (7), 1-17.
72. Liu, D.; Lv, Y.; Zhang, M.; Liu, Y.; Zhu, Y.; Zong, R.; Zhu, Y., *J. Mater. Chem. A* **2014**, *2* (37), 15377-15388.
73. Zhu, A.; Zhang, J.; Guan, F.; Tang, H.; Feng, X., *ACS omega* **2019**, *4* (2), 3534-3538.
74. Xia, T.; Wang, Y.; Mai, C.; Pan, G.; Zhang, L.; Zhao, W.; Zhang, J., *RSC Adv.* **2019**, *9* (34), 19253-19260.
75. Huang, X.; Xia, X.; Yuan, Y.; Zhou, F., *Electrochim. Acta* **2011**, *56* (14), 4960-4965.
76. Yin, X.; Wang, Y.; Jacobs, R.; Shi, Y.; Szlufarska, I.; Morgan, D.; Wang, X., *Nano Lett.* **2019**, *19* (10), 7085-7092.
77. Jung, M.-H.; Chu, M.-J., *J. Mater. Chem. C* **2014**, *2* (32), 6675-6682.
78. Zhang, X. L.; Qiao, R.; Qiu, R.; Kim, J. C.; Kang, Y. S., *Cryst. Growth Des.* **2009**, *9* (6), 2906-2910.
79. Sun, Z.; Liao, T.; Dou, Y.; Hwang, S. M.; Park, M.-S.; Jiang, L.; Kim, J. H.; Dou, S. X., *Nat. Commun.* **2014**, *5* (1), 1-9.
80. Zhang, Y.; Liu, C.; Gong, F.; Jiu, B.; Li, F., *Mater. Lett.* **2017**, *186*, 7-11.

81. Xiao, Y.; Lu, L.; Zhang, A.; Zhang, Y.; Sun, L.; Huo, L.; Li, F., *ACS Appl. Mater. Interfaces* **2012**, 4 (8), 3797-3804.
82. Du, J.; Zhao, R.; Chen, S.; Wang, H.; Li, J.; Zhu, Z., *ACS Appl. Mater. Interfaces* **2015**, 7 (10), 5870-5878.
83. Hou, C.; Zhang, M.; Zhang, L.; Tang, Y.; Wang, H.; Chi, Q., *Chem. Mater.* **2017**, 29 (3), 1439-1446.
84. Tom, K. B.; Lin, S.; Wan, L. F.; Wang, J.; Ahlm, N.; N'Diaye, A. T.; Bustillo, K.; Huang, J.; Liu, Y.; Lou, S., *ACS Nano* **2018**, 12 (8), 7554-7561.
85. Liu, F.; Wang, X.; Chen, X.; Song, X.; Tian, J.; Cui, H., *ACS Appl. Mater. Interfaces* **2019**, 11 (27), 24757-24763.
86. Wang, P.; Wang, D.; Zhang, M.; Zhu, Y.; Xu, Y.; Ma, X.; Wang, X., *Sens. Actuators B Chem.* **2016**, 230, 477-484.
87. Wang, Z.; Gan, L.; He, H.; Ye, Z., *ACS Appl. Mater. Interfaces* **2017**, 9 (15), 13537-13543.
88. Zhou, Y.; Chen, G.; Yu, Y.; Yan, C.; Sun, J.; He, F., *J. Phys. Chem.* **2016**, 4 (3), 781-784.
89. Zhu, A.; Zhang, J.; Guan, F.; Tang, H.; Feng, X., *ACS omega* **2019**, 4 (2), 3534-3538.
90. Phuruangrat, A.; Thongtem, S.; Thongtem, T., *Mater. Des.* **2016**, 107, 250-256.
91. Xu, J.; Xue, Z.; Qin, N.; Cheng, Z.; Xiang, Q., *Sens. Actuators B Chem.* **2017**, 242, 148-157.
92. Zhang, X.; Zhang, J.; Zhao, J.; Pan, B.; Kong, M.; Chen, J.; Xie, Y., *J. Am. Chem. Soc.* **2012**, 134 (29), 11908-11911.
93. Chen, M.; Wang, Z.; Han, D.; Gu, F.; Guo, G., *J. Phys. Chem. C* **2011**, 115 (26), 12763-12773.
94. Yu, L.; Wei, J.; Luo, Y.; Tao, Y.; Lei, M.; Fan, X.; Yan, W.; Peng, P., *Sens. Actuators B Chem.* **2014**, 204, 96-101.
95. Yu, L.; Guo, F.; Liu, S.; Yang, B.; Jiang, Y.; Qi, L.; Fan, X., *J. Alloys Compd.* **2016**, 682, 352-356.
96. Wang, L.; Liu, S.; Zhang, Z.; Feng, X.; Zhu, L.; Guo, H.; Ding, W.; Chen, L.; Qin, Y.; Wang, Z. L., *Nano Energy* **2019**, 60, 724-733.
97. Abinaya, S.; Kavitha, H. P.; Prakash, M.; Muthukrishnaraj, A., *Sustainable Chemistry and Pharmacy* **2021**, 19, 100368.
98. Lee, Y.; Kim, S.; Kim, D.; Lee, C.; Park, H.; Lee, J.-H., *Appl. Surf. Sci.* **2020**, 509, 145328.
99. Kumar, M.; Bhatt, V.; Kim, J.; Abhyankar, A. C.; Chung, H.-J.; Singh, K.; Cho, Y. B.; Yun, Y. J.; Lim, K. S.; Yun, J.-H., *Sens. Actuators B Chem.* **2021**, 326, 128839.
100. Guo, Q.; Fu, L.; Yan, T.; Tian, W.; Ma, D.; Li, J.; Jiang, Y.; Wang, X., *Appl. Surf. Sci.* **2020**, 509, 144773.
101. Gao, S.; Yang, F.; Song, C.; Cai, Q.; Wang, R.; Zhou, S.; Kong, Y., *Appl. Surf. Sci.* **2020**, 505, 144580.
102. Shi, W.; Ahmed, M. M.; Li, S.; Shang, Y.; Liu, R.; Guo, T.; Zhao, R.; Li, J.; Du, J., *ACS Appl. Nano Mater.* **2019**, 2 (9), 5430-5439.
103. Zhou, H.; Liu, P.; Du, J.; Wang, F.; Wang, X.; Du, X., *Anal. Methods* **2020**, 12 (42), 5086-5096.
104. Gupta, S. P.; Pawbake, A. S.; Sathe, B. R.; Late, D. J.; Walke, P. S., *Sens. Actuators B Chem.* **2019**, 293, 83-92.
105. Banerjee, A.; Chattopadhyay, S.; Kundu, A.; Sharma, R. K.; Maiti, P.; Das, S., *Ceram. Int.* **2019**, 45 (14), 16821-16828.
106. Shi, Q.; Cheng, W. J. A. F. M., *Adv. Funct. Mater.* **2020**, 30 (2), 1902301.
107. Rao, S.; Si, K. J.; Yap, L. W.; Xiang, Y.; Cheng, W. J. A. n., *ACS Nano* **2015**, 9 (11), 11218-11224.
108. Wang, F.; Seo, J.-H.; Ma, Z.; Wang, X., *ACS Nano* **2012**, 6 (3), 2602-2609.
109. Murphy, C. J.; Sau, T. K.; Gole, A. M.; Orendorff, C. J.; Gao, J.; Gou, L.; Hunyadi, S. E.; Li, T. J. T. J. o. P. C. B., *J. Phys. Chem.* **2005**, 109 (29), 13857-13870.
110. M. B. B.; Manippady, S. R.; Saxena, M.; B, R. P.; John, N. S.; Balakrishna, R. G.; Samal, A. K., *Langmuir* **2020**, 36 (26), 7332-7344.
111. Yin, X.; Chen, Q.; Tian, P.; Zhang, P.; Zhang, Z.; Voyles, P. M.; Wang, X., *Chem. Mater.* **2018**, 30 (10), 3308-3314.
112. Wang, F.; Jakes, J. E.; Geng, D.; Wang, X., *ACS Nano* **2013**, 7 (7), 6007-6016.
113. Ding, Y.; Yang, R.; Wang, Z. L., *Solid State Commun.* **2006**, 138 (8), 390-394.
114. Wang, F.; Yin, X.; Wang, X., *Extreme Mech. Lett.* **2016**, 7, 64-70.
115. Yin, X.; Shi, Y.; Wei, Y.; Joo, Y.; Gopalan, P.; Szlufarska, I.; Wang, X., *Langmuir* **2017**, 33 (31), 7708-7714.
116. Xia, Y.; Xiong, Y.; Lim, B.; Skrabalak, S. E. J. A. C. I. E., *Angew. Chem., Int. Ed.* **2009**, 48 (1), 60-103.
117. Jin, S.; Bierman, M. J.; Morin, S. A. J. T. J. o. P. C. L., *J. Phys. Chem. Lett.* **2010**, 1 (9), 1472-1480.
118. Morin, S. A.; Forticaux, A.; Bierman, M. J.; Jin, S., *Nano Lett.* **2011**, 11 (10), 4449-4455.
119. Wang, Y.; Shi, Y.; Zhang, Z.; Carlos, C.; Zhang, C.; Bhawnani, K.; Li, J.; Wang, J.; Voyles, P. M.; Szlufarska, I., *Chem. Mater.* **2019**, 31 (21), 9040-9048.
120. Zhuang, Z.; Peng, Q.; Li, Y., *Chem. Soc. Rev.* **2011**, 40 (11), 5492-5513.
121. Simon, P.; Bahrig, L.; Baburin, I. A.; Formanek, P.; Röder, F.; Sickmann, J.; Hickey, S. G.; Eychmüller, A.; Lichte, H.; Kniep, R., *Adv. Mater.* **2014**, 26 (19), 3042-3049.
122. Wang, Z.; Schliehe, C.; Wang, T.; Nagaoka, Y.; Cao, Y. C.; Bassett, W. A.; Wu, H.; Fan, H.; Weller, H., *J. Am. Chem. Soc.* **2011**, 133 (37), 14484-14487.
123. Zhang, L.; Zhao, J.; Lu, H.; Li, L.; Zheng, J.; Li, H.; Zhu, Z., *Sens. Actuators B Chem.* **2012**, 161 (1), 209-215.

124. Evers, W. H.; Goris, B.; Bals, S.; Casavola, M.; De Graaf, J.; Van Roij, R.; Dijkstra, M.; Vanmaekelbergh, D. I., *Nano Lett.* **2013**, *13* (6), 2317-2323.
125. Yu, T.; Lim, B.; Xia, Y., *Angew. Chem.* **2010**, *122* (26), 4586-4589.
126. Chen, X.; Zhou, Y.; Liu, Q.; Li, Z.; Liu, J.; Zou, Z., *ACS Appl. Mater. Interfaces* **2012**, *4* (7), 3372-3377.
127. Sahu, K.; Choudhary, S.; Singh, J.; Kuriakose, S.; Singhal, R.; Mohapatra, S., *Ceram. Int.* **2018**, *44* (18), 23094-23101.
128. Wang, L.-P.; Jin, Z.; Luo, T.; Ding, Y.; Liu, J.-H.; Wang, X.-F.; Li, M.-Q., *New J. Chem.* **2019**, *43* (8), 3619-3624.
129. Fan, Z.; Zhang, H., *Acc. Chem. Res.* **2016**, *49* (12), 2841-2850.
130. Liu, Y.; Goebel, J.; Yin, Y., *Chem. Soc. Rev.* **2013**, *42* (7), 2610-2653.
131. Liu, J.; Hu, Z.-Y.; Peng, Y.; Huang, H.-W.; Li, Y.; Wu, M.; Ke, X.-X.; Van Tendeloo, G.; Su, B.-L., *Appl. Catal. B* **2016**, *181*, 138-145.
132. Shi, Y.; Li, H.; Li, L.-J., *Chem. Soc. Rev.* **2015**, *44* (9), 2744-2756.
133. Johnson, R. W.; Hultqvist, A.; Bent, S. F. J. M. t., *Mater. Today* **2014**, *17* (5), 236-246.
134. Naeem, F.; Naeem, S.; Zhao, Z.; Shu, G.-q.; Zhang, J.; Mei, Y.; Huang, G. J. J. o. P. S., *Journal of Power Sources* **2020**, *451*, 227740.
135. Yang, Z.; Hao, J. J. J. o. M. C. C., *J. Mater. Chem. C* **2016**, *4* (38), 8859-8878.
136. Weigand, C.; Bergren, M.; Ladam, C.; Tveit, J.; Holmestad, R.; Vullum, P.; Walmsley, J.; Dahl, Ø.; Furtak, T.; Collins, R., *Cryst. Growth Des.* **2011**, *11* (12), 5298-5304.
137. Zhang, H., *ACS Nano* **2015**, *9* (10), 9451-9469.
138. Khan, Z.; Singh, P.; Ansari, S. A.; Manippady, S. R.; Jaiswal, A.; Saxena, M., *Small* **2021**, *17* (4), 2006651.
139. Khan, Z.; Ail, U.; Nadia Ajjan, F.; Phopase, J.; Ullah Khan, Z.; Kim, N.; Nilsson, J.; Inganäs, O.; Berggren, M.; Crispin, X., *Advanced Energy and Sustainability Research* **2022**, *3* (1), 2100165.
140. Ajjan, F. N.; Khan, Z.; Riera-Galindo, S.; Lienemann, S.; Vagin, M.; Petsagkourakis, I.; Gabrielsson, R.; Braun, S.; Fahlman, M.; Inganäs, O.; Berggren, M.; Crispin, X., *Advanced Energy and Sustainability Research* **2020**, *1* (2), 2000027.
141. Khan, Z.; Ail, U.; Ajjan, F. N.; Phopase, J.; Kim, N.; Kumar, D.; Khan, Z. U.; Nilsson, J.; Inganäs, O.; Berggren, M.; Crispin, X., *Journal of Power Sources* **2022**, *524*, 231103.
142. Khan, Z.; Vagin, M.; Crispin, X. J. a. s., *Adv. Sci.* **2020**, *7* (5), 1902866.
143. Etacheri, V.; Marom, R.; Elazari, R.; Salitra, G.; Aurbach, D., *Energy Environ. Sci.* **2011**, *4* (9), 3243-3262.
144. Chen, D.; Chen, W.; Ma, L.; Ji, G.; Chang, K.; Lee, J. Y., *Mater. Today* **2014**, *17* (4), 184-193.
145. Shi, L.; Zhao, T., *J. Mater. Chem. A* **2017**, *5* (8), 3735-3758.
146. Pumera, M.; Sofer, Z.; Ambrosi, A., *J. Mater. Chem. A* **2014**, *2* (24), 8981-8987.
147. Ji, L.; Lin, Z.; Alcoutlabi, M.; Zhang, X., *Energy Environ. Sci.* **2011**, *4* (8), 2682-2699.
148. Cao, X.; Zheng, B.; Rui, X.; Shi, W.; Yan, Q.; Zhang, H., *Angew. Chem., Int. Ed.* **2014**, *53* (5), 1404-1409.
149. Zhang, W.-J., *J. Power Sources* **2011**, *196* (1), 13-24.
150. Jing, Y.; Zhou, Z.; Cabrera, C. R.; Chen, Z., *J. Mater. Chem. A* **2014**, *2* (31), 12104-12122.
151. Meng, C.; Das, P.; Shi, X.; Fu, Q.; Müllen, K.; Wu, Z.-S. J. S. S., *Small Sci.* **2021**, *1* (4), 2000076.
152. Xie, X.; Liang, S.; Gao, J.; Guo, S.; Guo, J.; Wang, C.; Xu, G.; Wu, X.; Chen, G.; Zhou, J., *Energy Environ. Sci.* **2020**, *13* (2), 503-510.
153. Kim, J. Y.; Liu, G.; Shim, G. Y.; Kim, H.; Lee, J. K., **2020**, *30* (36), 2004210.
154. Simon, P.; Gogotsi, Y., *Materials for electrochemical capacitors*. In *Nanoscience and technology: a collection of reviews from Nature journals*, World Scientific: 2010; pp 320-329.
155. Wang, Q.; O'Hare, D., *Chem. Rev.* **2012**, *112* (7), 4124-4155.
156. Cai, X.; Luo, Y.; Liu, B.; Cheng, H.-M., *Chem. Soc. Rev.* **2018**, *47* (16), 6224-6266.
157. Jung, M.-H.; Lee, H., *Nanoscale Res. Lett.* **2011**, *6* (1), 159.
158. Balakrishna Pillai, P.; Kumar, A.; Song, X.; De Souza, M. M., *ACS Appl. Mater. Interfaces* **2018**, *10* (11), 9782-9791.
159. Khokhra, R.; Bharti, B.; Lee, H.-N.; Kumar, R., *Sci. Rep.* **2017**, *7* (1), 1-14.
160. Ran, J.; Zhang, J.; Yu, J.; Jaroniec, M.; Qiao, S. Z., *Chem. Soc. Rev.* **2014**, *43* (22), 7787-7812.
161. Chen, Z.; Jaramillo, T. F.; Deutsch, T. G.; Kleiman-Shwarscstein, A.; Forman, A. J.; Gaillard, N.; Garland, R.; Takanabe, K.; Heske, C.; Sunkara, M., *J. Mater. Res.* **2010**, *25* (1), 3.
162. Qi, K.; Cheng, B.; Yu, J.; Ho, W. J. J. o. A.; Compounds, *J. Alloys Compd.* **2017**, *727*, 792-820.
163. Chamangard, N.; Asgharzadeh, H., *CrystEngComm* **2016**, *18* (47), 9103-9112.
164. Dral, A. P.; Johan, E., *Sens. Actuators B Chem.* **2018**, *272*, 369-392.
165. Wang, H.; Rogach, A. L., *Chem. Mater.* **2014**, *26* (1), 123-133.
166. Wang, X.; He, X.; Zhu, H.; Sun, L.; Fu, W.; Wang, X.; Hoong, L. C.; Wang, H.; Zeng, Q.; Zhao, W., *Sci. Adv.* **2016**, *2* (7), e1600209.
167. Varghese, S. S.; Varghese, S. H.; Swaminathan, S.; Singh, K. K.; Mittal, V., *Electron.* **2015**, *4* (3), 651-687.
168. Yang, W.; Gan, L.; Li, H.; Zhai, T., *Inorg. Chem. Front.* **2016**, *3* (4), 433-451.
169. Wang, J.; Yang, J.; Han, N.; Zhou, X.; Gong, S.; Yang, J.; Hu, P.; Chen, Y., *Mater. Des.* **2017**, *121*, 69-76.
170. Hjiri, M.; El Mir, L.; Leonardi, S. G.; Donato, N.; Neri, G., *Nanomaterials* **2013**, *3* (3), 357-369.
171. Ju, D.; Xu, H.; Zhang, J.; Guo, J.; Cao, B., *Sens. Actuators B Chem.* **2014**, *201*, 444-451.
172. Meng, Z.; Stolz, R. M.; Mendecki, L.; Mirica, K. A., *Chem. Rev.* **2019**, *119* (1), 478-598.
173. Xiao, C.; Yang, T.; Chuai, M.; Xiao, B.; Zhang, M., *Phys. Chem. Chem. Phys.* **2016**, *18* (1), 325-330.
174. Mun, Y.; Park, S.; An, S.; Lee, C.; Kim, H. W., *Ceram. Int.* **2013**, *39* (8), 8615-8622.

175. Wang, Z. L., *Adv. Mater.* **2007**, *19* (6), 889-892.
176. Wang, Z. L., *Nano Today* **2010**, *5* (6), 540-552.
177. Wang, Z. L.; Wu, W., *Natl. Sci. Rev.* **2014**, *1* (1), 62-90.
178. Wu, W.; Wen, X.; Wang, Z. L., *Science* **2013**, *340* (6135), 952-957.
179. Wu, W.; Wei, Y.; Wang, Z. L., *Adv. Mater.* **2010**, *22* (42), 4711-4715.
180. Liu, S.; Wang, L.; Feng, X.; Wang, Z.; Xu, Q.; Bai, S.; Qin, Y.; Wang, Z. L., *Adv. Mater.* **2017**, *29* (16), 1606346.
181. Wang, L.; Liu, S.; Feng, X.; Xu, Q.; Bai, S.; Zhu, L.; Chen, L.; Qin, Y.; Wang, Z. L., *ACS Nano* **2017**, *11* (5), 4859-4865.
182. Dong, L.; Lou, J.; Shenoy, V. B., *ACS Nano* **2017**, *11* (8), 8242-8248.
183. Brennan, C. J.; Ghosh, R.; Koul, K.; Banerjee, S. K.; Lu, N.; Yu, E. T., *Nano Lett.* **2017**, *17* (9), 5464-5471.
184. Syed, N.; Zavabeti, A.; Ou, J. Z.; Mohiuddin, M.; Pillai, N.; Carey, B. J.; Zhang, B. Y.; Datta, R. S.; Jannat, A.; Haque, F., *Nat. Commun.* **2018**, *9* (1), 1-10.
185. Scrymgeour, D. A.; Hsu, J. W., *Nano Lett.* **2008**, *8* (8), 2204-2209.
186. An, C.; Qi, H.; Wang, L.; Fu, X.; Wang, A.; Wang, Z. L.; Liu, J., *Nano Energy* **2021**, *82*, 105653.